On the influence of microstructure on fracture behaviour of hot extruded ferritic ODS steels

Das, A.; Viehrig, H. W.; Altstadt, E.; Heintze, C.; Hoffmann, J.;

Originally published:

November 2017

Journal of Nuclear Materials 497(2017), 60-75

DOI: https://doi.org/10.1016/j.jnucmat.2017.10.051

Perma-Link to Publication Repository of HZDR:

https://www.hzdr.de/publications/Publ-26055

On the influence of microstructure on fracture behaviour of hot extruded ferritic ODS steels

A. Das[1,a] , H.W. Viehrig[a], E. Altstadt[a], C. Heintze[a], J. Hoffmann[b]

[a] Helmholtz-Zentrum Dresden-Rossendorf, Bautzner Landstrasse 400, 01328 Dresden (Germany)

[b] Institute for Applied Materials, Karlsruhe Institute of Technology, Hermann-von-Helmholtz-Platz 1, 76344 Eggenstein-Leopoldshafen, Germany

[1)] Corresponding author, e-mail: a.das@hzdr.de

Abstract

ODS steels are known to show inferior fracture properties as compared to ferritic martensitic non-ODS steels. Hot extruded 13Cr ODS steel however, showed excellent fracture toughness at a temperature range from room temperature to 400 ˚C. In this work, the factors which resulted in superior and anisotropic fracture behaviour were investigated by comparing different orientations of two hot extruded materials using scanning electron, electron backscatter and transmission electron microscopy. Fracture behaviour of the two materials was compared using unloading compliance fracture toughness tests. Anisotropic fracture toughness was predominantly influenced by grain morphology. Superior fracture toughness in 13Cr ODS-KIT was predominantly influenced by factors such as smaller void inducing particle size and higher sub-micron particle-matrix interfacial strength.

Keywords

ODS-steel, fracture behaviour, fracture toughness, anisotropy, bimodal microstructure, fractography, ductile fracture, void growth and coalescence, critical fracture strain, ductility, void inducing particles

Highlights

- Superior fracture toughness in ODS-KIT from RT to 400 ˚C was obtained due to dominant effect of high interfacial particle-matrix strength and small size of sub-micron particles
- Crack blunting due to elongated coarse grains contributes predominantly towards improving fracture toughness in the strongest orientation
- Crystallographic texture is not the dominant contributor to fracture toughness
- Sub-micron particle properties do not play a major role in fracture toughness anisotropy

1 Introduction

Oxide dispersion strengthened (ODS) steels are known for their high temperature strength [1,2] and irradiation swelling resistance [3]. Two variants of ODS steels have been the most prolific, the ferritic/martensitic ones with Cr content in the range of 9-12 weight% and the ferritic ones with Cr content in the range of 12-20 weight%. Ferritic ODS steels have higher corrosion resistance and do not go through any phase transformation at high temperatures. Fracture toughness is an important characteristic of a material which determines its structural integrity, workability and load absorption capability over different temperature ranges. In general, ODS steels possess lower fracture toughness than non-ODS ferritic martensitic (FM) steels [4,5] at room temperature. The difference can be even more pronounced at higher temperatures [5]. 13Cr hot extruded ODS steel from Karlsruhe Institute of technology (KIT) however, compared to other ODS steels, exhibited superior fracture toughness at a temperature range of room temperature till 400 ˚C. Fracture toughness anisotropy was also observed. This work investigates the factors responsible for its superior and anisotropic fracture toughness.

Hot extrusion is a commonly used technique for manufacturing rods of ODS steels. Hot extruded rods contain similar anisotropic microstructural features as cold pilgering, a process used to make cladding tubes in Gen-IV nuclear fission reactors [6]. The anisotropic microstructure gives rise to an anisotropic fracture behaviour as earlier observed for specimens made from hot extrusion [7–11]. The possible reasons for this behaviour are believed to be anisotropic grain morphology and crystallographic orientation.

In this work, the factors which affect the fracture behaviour of two hot extruded ODS steels (13Cr KIT and 14Cr CSM) were investigated. Fracture toughness tests using miniature compact tension specimens (C(T)) were performed from room temperature till 600 ˚C in three orientations. Scanning electron microscopy (SEM) was performed on primary crack fracture surfaces to reveal more information about the mode of fracture. Electron backscatter diffraction (EBSD) was used to investigate bulk microstructure as well as crack propagation. Transmission electron microscopy (TEM) investigations were performed to know more about the particle distributions with respect to the grains.

Through this investigation, a correlation between anisotropic variations in fracture toughness of ODS-KIT and its anisotropic microstructural features such as crystallographic orientation, void inducing particles and grain morphology is established. A comparison of the two hot extruded materials with respect to their fracture toughness and the factors affecting them is also performed. This throws light on the microstructural features which dominantly contribute to the superior fracture toughness of ODS-KIT in the ductile regime.

2 Materials and methods

2.1 Material

Hot extruded 13% Cr ODS steel rod was provided by Karlsruhe Institute of Technology, Germany (KIT). The bulk chemical composition of the extruded rod, presented in Table 1, was obtained using optical emission spectrometry (Thermo Scientific ARL 8860) from BGH Edelstahl Freital GmbH, Germany. The main production steps were: mechanical alloying in an attritor ball mill, encapsulation of the powder, evacuation of the capsule and hot extrusion at 1100 °C. Details of the production can be found in reference [12].

Hot extruded 14% Cr ODS steel rod was provided by Centro Sviluppo Materiali, Italy (CSM). Gas atomized pre-alloyed steel matrix was added with 0.3% Y_2O_3 and dry ball milled in an environment of Ar and H. After canning, direct hot extrusion was performed at 1150 ˚C with an extrusion ratio of 22.5. Heat treatment was performed at 1050 °C for one hour and then cooled in the furnace. The bulk chemical composition of the hot extruded material is presented in Table 1.

Table 1 Bulk chemical composition of the investigated ODS alloys (wt.%)

Elements	ODS-KIT HE	ODS-CSM
Fe	85.28	83.84
Cr	12.99	13.76
W	1.03	0.842
V	0.007	0.012
Ti	0.138	0.238
Si	0.051	0.371
Al	0.009	0.027
Ni	0.101	0.239
Cu	0.017	0.012
Mn	0.088	0.056
Zr	0.037	0.047
P	0.01	0.006
N	0.009	0.166
C	0.028	0.01
O	0.002	0.003
Y	0.165	0.279

2.2 Fracture mechanics specimens

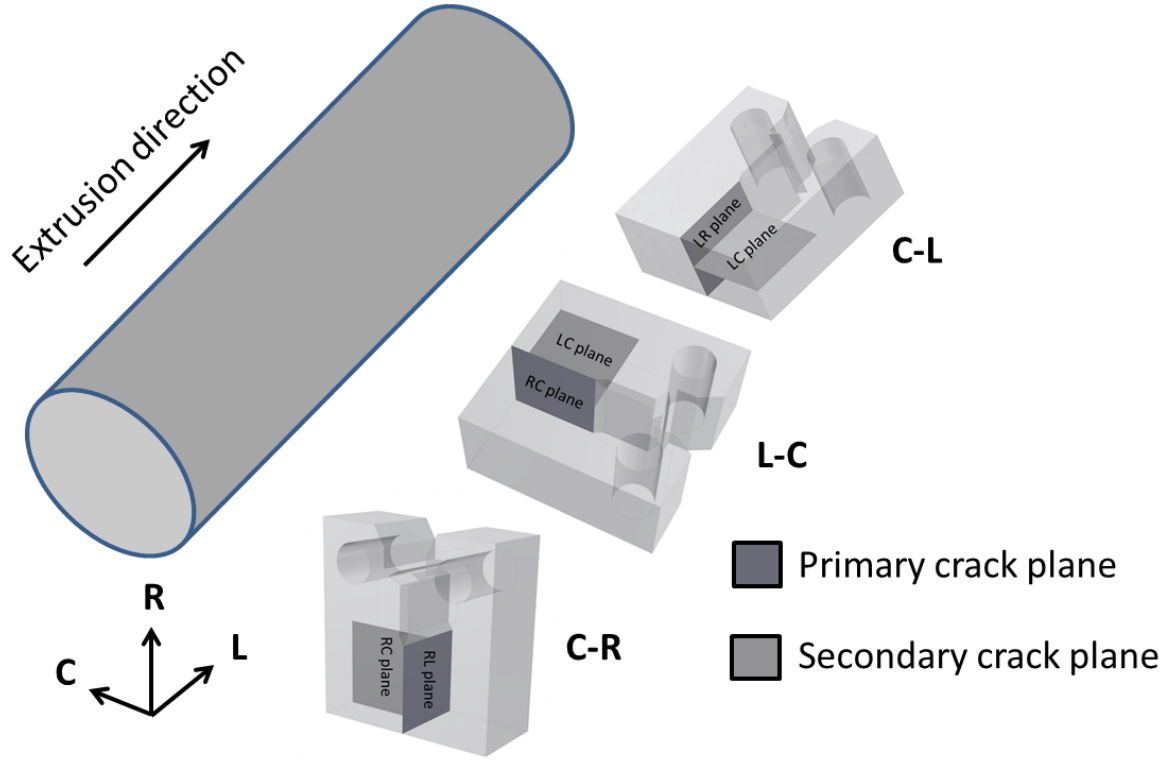

Fig. 1 Cutting scheme for the C-R, L-C and C-L oriented specimens indicating primary and secondary crack planes

Miniature compact tension C(T) specimen of 4 mm thickness (0.16T) were machined from both the materials. The cutting scheme of the specimens along with the different orientations can be seen in Fig. 1. All the C(T) specimens were 20% side grooved and fatigue pre-cracked at room temperature to a crack length to width ratio (a/W) of 0.5 using a resonance testing machine. The nominal cyclic stress intensity at the end of fatigue pre-cracking stage (K_{end}) was 14 MPa√m.

2.3 Quasi-static fracture toughness testing

Quasi-static fracture toughness tests were carried out on small size C(T) specimens in the L-C, C-R and C-L orientations using the unloading compliance method [13]. The unloadings were done with 25% load drop and 30 s relaxation time. Single tests were done at 22, 200, 400, 600 ˚C in air for 13%Cr ODS-KIT and two tests were performed for each temperature in case of 14%Cr ODS-CSM. The crosshead speed of the machine was 0.1 mm per minute with unloading steps of 0.015 mm. The tests were stopped after about 1 mm crack propagation and thereafter the specimens were heat tinted. The initial and the final primary crack lengths were measured at the fracture surfaces using optical microscope according to the nine point standard ASTM method [14]. The crack opening displacement (COD) measurements were done on load line using a contact clip on gauge in the temperature range from RT to 200 ˚C. From 200 ˚C to 600 ˚C, a contactless video extensometer was used at front face. Here, the compliance and displacement values were converted to the load line values [15]. Thereafter the evaluation was performed according to ASTM E1820-13 [14].

2.4 Tensile tests

Tensile tests were performed using miniature flat tensile test specimens with their gauge length parallel to the extrusion direction. The cross-section of the samples was 1 mm · 2 mm

with an overall length of 20 mm. Tests were carried out at temperatures varying from 20 ˚C to 700 ˚C. The tests were performed in air with a cross head speed of 0.1 mm/min. For ODS-KIT, 3 samples were tested at each temperature while for ODS-CSM, 1 sample was tested at each temperature.

2.5 Microscopy

Basic characterization

Back scattered mode in SEM was used on OP-S polished samples (10-30% amorphous silica, 50-70% water, 5-20% 1,3 butanediol) to obtain grain contrast and information about submicron particle alignment. Most particles however, fell out of the sample during OP-S polishing and holes of similar size were left behind. Electron back scatter diffraction (EBSD) was performed on OP-S polished samples to obtain information about crystallographic texture and grain distribution. A step size varying from 48 nm to 0.19 µm was used with a pixel resolution of 800 X 600 (20 kV accelerating voltage and 18 mm working distance). The exposure time varied from 7 to 12 ms. A misorientation angle of 10˚ was chosen to identify high angle grain boundaries during grain distribution analysis.

TEM investigations were performed using a Talos F200X FEG-(S)TEM (FEI) operated at 200 keV. Samples were prepared by means of electropolishing in a Tenupol-5 in 5% perchloric acid in methanol at -60°C employing a voltage of 23 V. Bright field imaging and low magnification STEM imaging with a HAADF detector were performed to characterize the submicron particles and nano-oxides in terms of size and spatial distribution. Information on the composition of the particles was obtained by means of STEM-EDS mapping.

Fracture behaviour

Most of the C(T) specimens were broken open after fracture mechanics testing. Stereoscopic microscope imaging was performed on all fractured surfaces for macroscopic images. SEM was performed on all fracture surfaces for higher magnification images.

Some selected C(T) specimens were however, not broken open after the test. The side surfaces of the propagated crack in these specimens were OP-S polished and then EBSD was performed to obtain information on the crack propagation with respect to the grain distribution and morphology.

3 Results

3.1 Basic characterization of the microstructure

3.1.1 Grain structures

ODS-KIT

The grain distribution maps along with quality maps of the longitudinal and transverse planes obtained for ODS-KIT are presented in Fig. 2a and b. They were extracted with a maximum misorientation angle of 10°, i.e. only high-angle grain boundaries (HAGBs) were considered. ODS-KIT contains zones of ‘cigar’ shaped coarse grains (> 3 µm) elongated in the extrusion direction with a grain aspect ratio (GAR) of 10 (Fig. 2b). These zones are parallel to the extrusion direction. The coarse grains are further divided into sub-grains (misorientation angle < 10°) with a size similar to the fine grains. The sub-grains are visible in the quality maps and in the TEM images (Fig. 2a and b and Fig. 6a). Additionally, zones of fine grains with a grain size of 0.2 µm to 3 µm were found. These zones are parallel to the extrusion

direction as well (Fig. 2b). The fine grains are only slightly elongated in extrusion direction with a GAR of 1.7 (Table 2).

A detailed statistical grain size analysis in terms of equivalent circular diameter (diameter of a circle with the same area as the grains), GAR and area fraction is presented in Table 2 and Table 3 for fine and coarse grains respectively. The distinction between fine and coarse grains was made at 3 μm based on the grain size distribution.

The inverse pole figure Z maps (IPF maps) shown in Fig. 3a and b show that the grains are preferentially oriented with the <110> direction parallel to the extrusion direction. There is no dominant texture perpendicular to the extrusion direction but weak textures of <111> and <001> can be seen in the inverse pole figures (IPFs) (Fig. 4a). The orientation distribution function (ODF) plots at a constant Euler angle of phi2 of 0˚ and 45˚ indicates dominant texture of {001} <110> along with a weak texture of {111} <112> [16] (Fig. 4b). There is no difference between the fine and the coarse grained regions in terms of texture.

ODS-CSM

ODS-CSM contains zones of fine grains (size range: 0.25 μm to 1.5 μm) and zones of moderately coarser grains (>1.5 μm) as can be seen from the grain distribution maps along with the quality maps in Fig. 2c and d as well as low magnification STEM imaging (Fig. 6c). Both these zones are parallel to the extrusion direction similar to the situation observed in ODS-KIT. The coarse and the fine grains are slightly elongated towards the extrusion direction with a GAR of 3.3 and 2, respectively (Fig. 2d).

The equivalent circular diameter, GAR and area fraction of the fine and coarse grains are presented in Table 2 and Table 3, respectively. The distinction between fine and coarse grains was made at 1.5 μm based on the size distribution.

The crystallographic texture, as shown in the inverse pole figure Z maps (Fig. 3c and d), is similar to ODS-KIT showing grains with the <110> direction preferentially oriented parallel to the extrusion direction. There is no dominant texture perpendicular to the extrusion direction with only a very weak texture of <111> and <110> directions as observed in the IPFs (Fig. 4c). The ODF plots at a constant Euler angle phi2 of 0˚ and 45˚ indicate the dominant texture of {001} <110> along with weak textures of {011} <100> and {111} <112> [16] (Fig. 4d). The fine and the coarse grained regions both have similar texture.

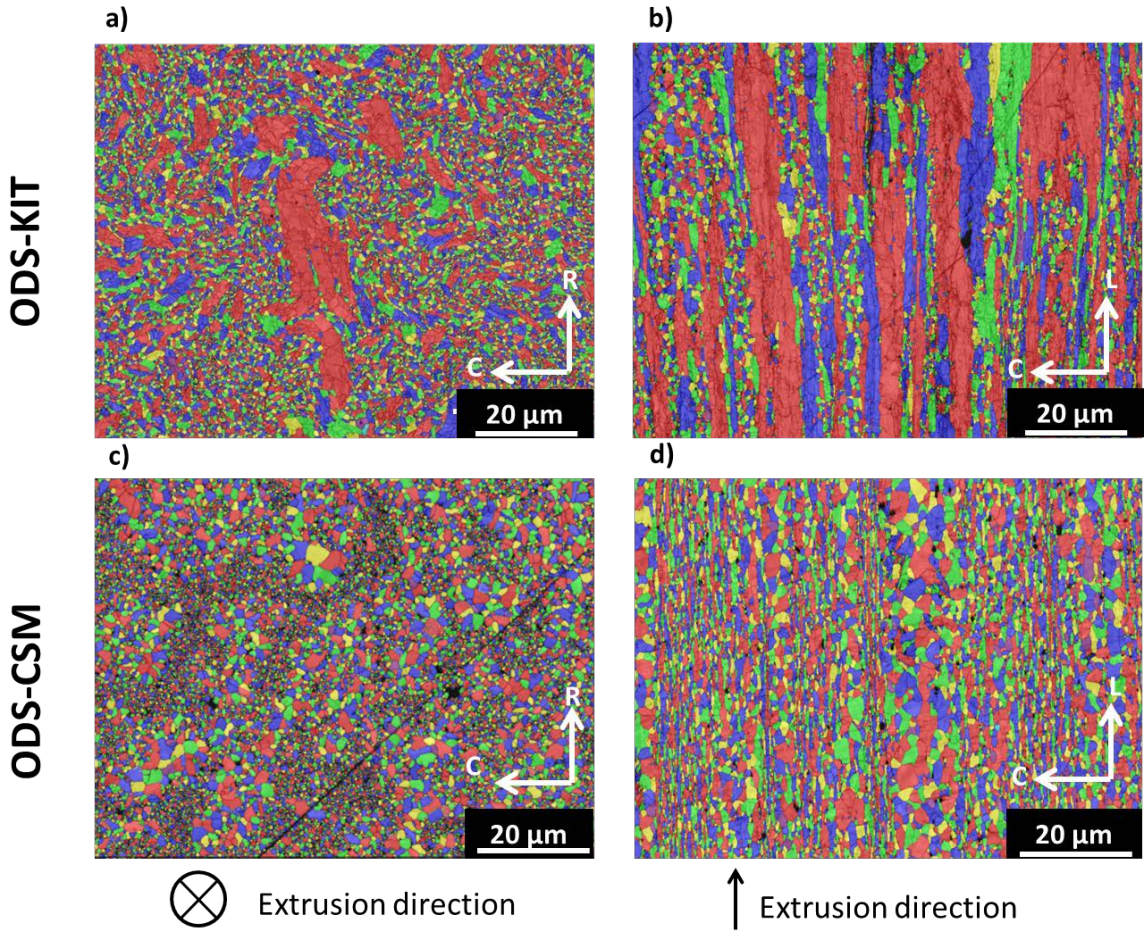

Fig. 2 Grain distribution maps along with quality maps (10˚ maximum misorientation angle) of the longitudinal (L, left) and the transversal (T, right) plane for ODS-KIT (a and b) and ODS-CSM (c and d). Indicated GAR values are for coarse grains.

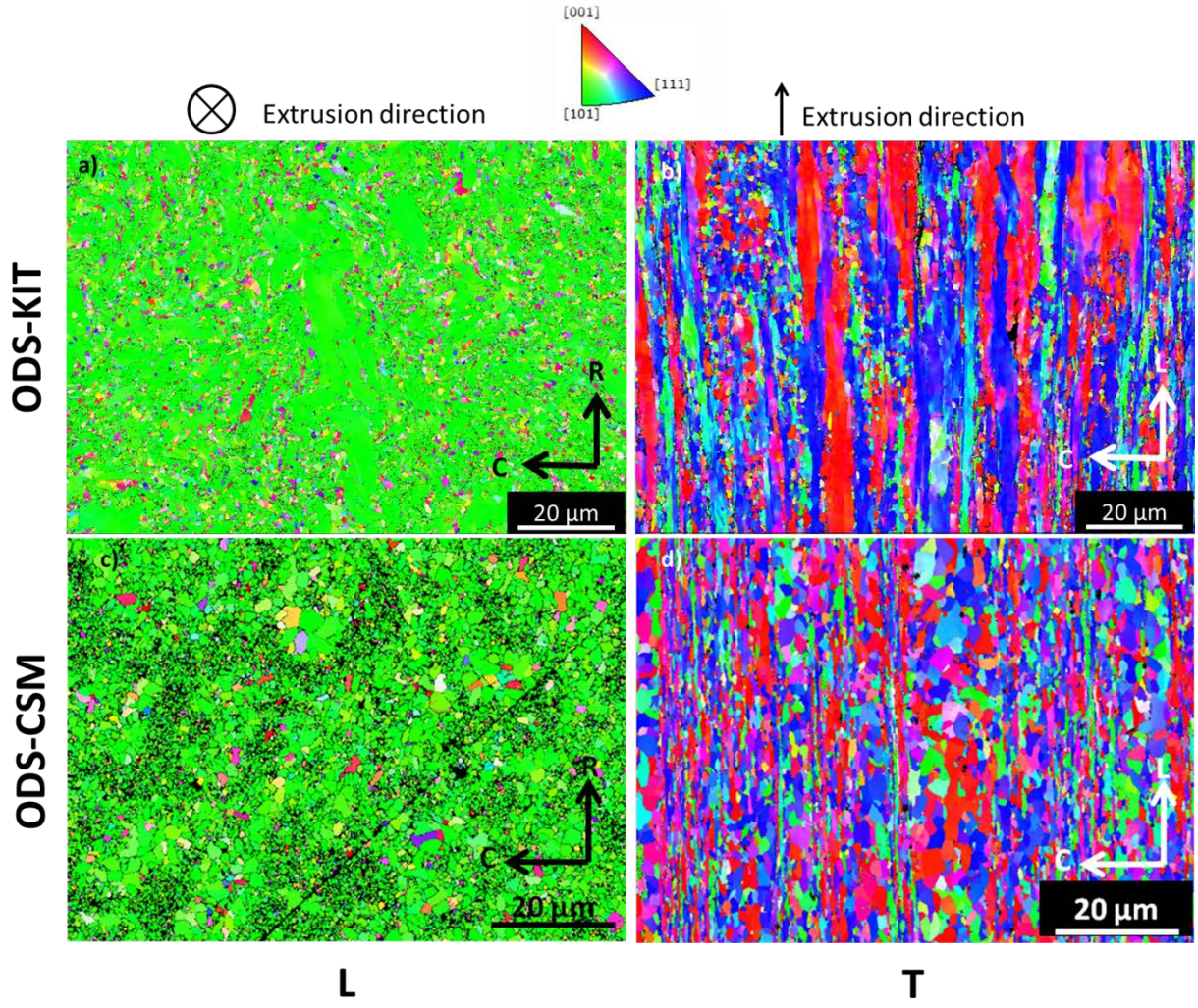

Fig. 3 Inverse pole figure Z maps of the longitudinal (L, left) and the transversal (T, right) plane for ODS-KIT (a and b) and ODS-CSM (c and d)

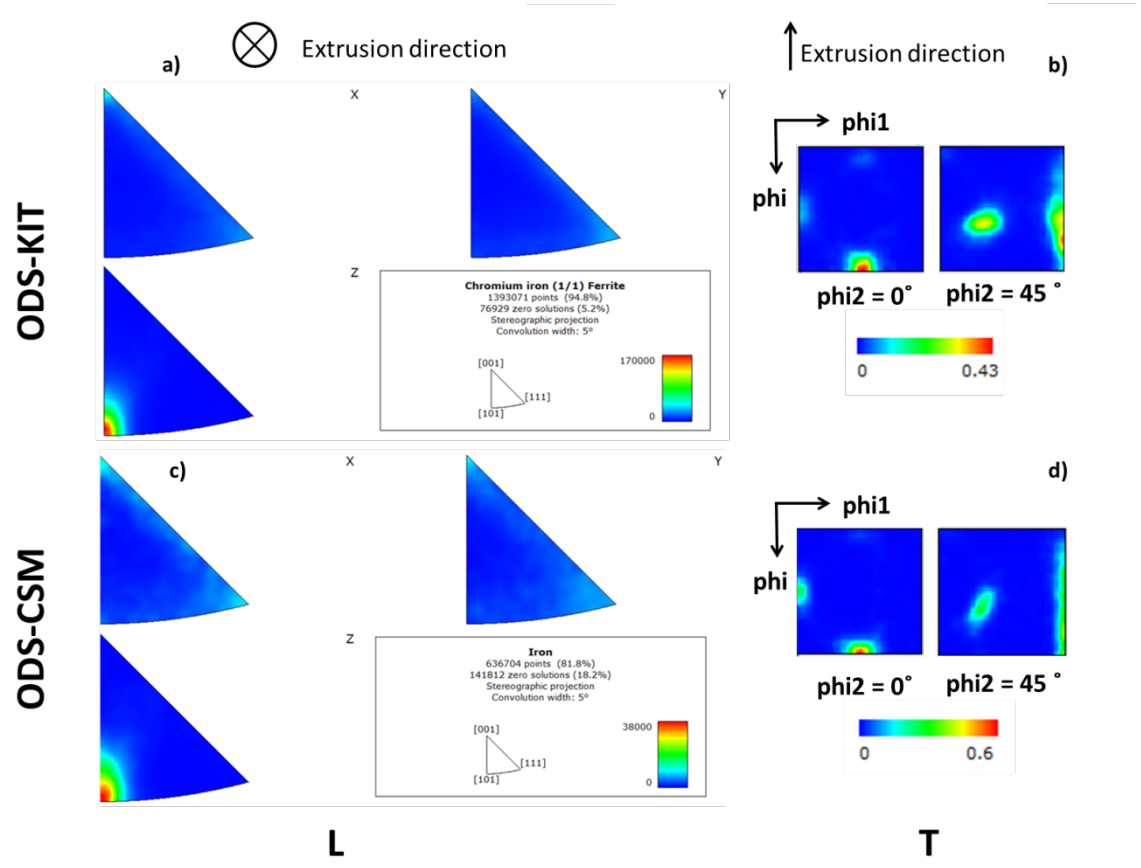

Fig. 4 IPF map in longitudinal direction (L) and ODF plots in Euler space at constant Euler angle phi2 of 0˚ and 45˚ in transverse direction (T) for ODS-KIT (a and b) and ODS-CSM (c and d)

Table 2 Grain size analysis for fine grains

Material	Plane	Equivalent grain diameter (µm)	GAR	Area fraction (%)
ODS-KIT	L (0.2 - 3 µm)	0.78	1.7	68.9
ODS-KIT	T (0.2 - 3 µm)	0.9	1.7	39.4
ODS-CSM	L (0.25 – 1.5 µm)	0.65	1.43	46
ODS-CSM	T (0.25 – 1.5 µm)	0.75	2	35.4

Table 3 Grain size analysis for coarse grains

Material	Plane	Equivalent grain diameter (µm)	GAR	Area fraction (%)
ODS-KIT	L (3 - 21 µm)	4.7	2.2	31.1
ODS-KIT	T (3 - 30 µm)	7.7	10	60.6
ODS-CSM	L (1.5 – 5 µm)	2.1	1.54	54
ODS-CSM	T (1.5 – 9.4 µm)	2.4	3.3	64.6

3.1.2 Particles

In the following, we distinguish sub-micron particles with sizes in the order of 100 nm up to 1 µm and nano-oxides of few to several nm. Although the latter are characteristic for ODS

steels, the focus is given to the sub-micron particles as they are more important from the viewpoint of fracture behaviour.

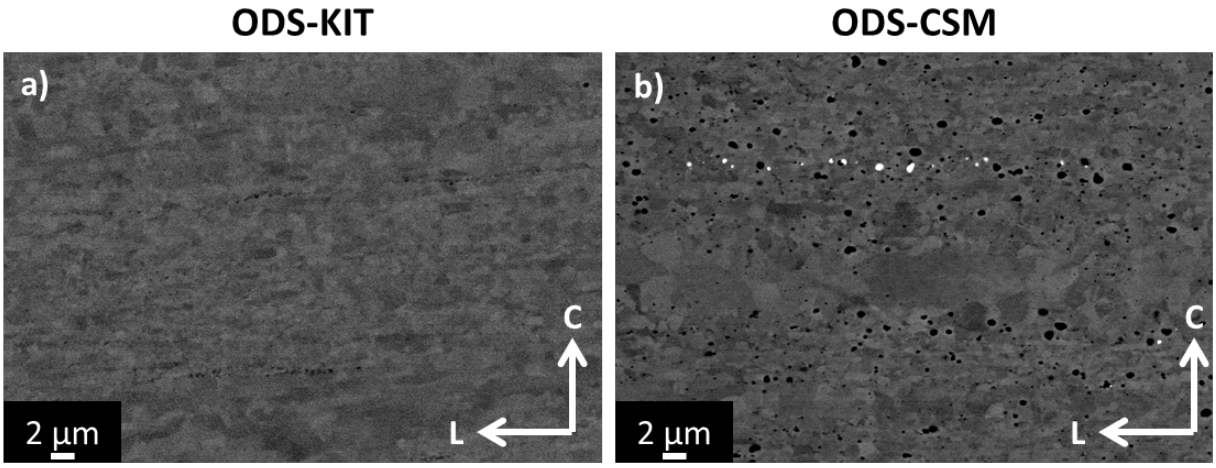

Fig. 5 SEM back scattered images of a) ODS-KIT and b) ODS-CSM showing grain contrast along with holes left out by sub-micron particles after OP-S polishing

ODS-KIT

Fig. 7 shows sub-micron particles with a size of 30 nm to 130 nm in ODS-KIT. They are located sometimes on the grain boundaries (Fig. 7a) and sometimes inside grains (Fig. 7b). Most of these particles are arranged in high density bands parallel to the extrusion direction (HD zones) covering a length of several µm and with a mean thickness of 0.4 µm (Fig. 7b). The mean spacing between individual bands is 7.6 µm (Fig. 5a). The particle density in the areas between these bands is low (LD zones). In Fig. 5a, one can observe the holes left out by the sub-micron particles during OP-S polishing. These are close to the resolvable limit using SEM. The mean particle size, the inter-particle spacing and the volume fraction of the sub-micron particles can be found in Table 4 as separate values for the HD and LD zones. STEM-EDS was performed to obtain information on the composition of the particles as shown in Fig. 7c and Fig. 8. The majority of the sub-micron particles are seen to be enriched with Ti which can be hypothesized as Ti oxides. Occasionally, the particles are also seen to be enriched with Al and/or Y particles. The Al possibly came from the powder after milling, as it is present in small quantities in the bulk composition (Table 1).

Additionally, Fig. 6b shows nano-oxides particles (< 10 nm) of an average size of 3 nm. The spatial distribution of the nano-oxides is inhomogeneous with no visible preference to grain boundaries.

Table 4 Sub-micron particle size analysis of low and high density regions of ODS-KIT and ODS-CSM

Material	Region	Mean Particle Size (µm)	Volume fraction	Inter-particle spacing (µm)
ODS-KIT	HD zone	0.06	0.038	0.22
ODS-KIT	LD zone	0.06	0.0027	0.87
ODS-CSM	HD zone	0.47	0.0134	2.93
ODS-CSM	LD zone	0.09	0.0016	1.65

ODS-CSM

Fig. 5b and Fig. 6c show larger sub-micron particles in the size range of 0.2 µm to 1.2 µm in ODS-CSM. In contrast to ODS-KIT, these are not arranged in bands. Here, zones of high (HD zones) and low density (LD zones) of sub-micron particles can be distinguished within which the particles are distributed rather homogeneously. These zones are parallel to the extrusion direction and have a mean thickness of 4.4 µm and 6 µm, respectively (Fig. 5b and Fig. 6c). The high density zones often coincide with the fine grained zones, while the low density zones often coincide with the coarse grained zones.

Fig. 9 shows STEM-EDS images revealing different types of sub-micron particles. The larger sub-micron particles (mean size 0.47 µm) can be identified as Si oxides. The smaller sub-micron particles (< 0.5 µm) include Y-oxides, Ti-oxides and oxides of more complex composition enriched in Y, Ti and Si. Additionally, Fig. 9 shows Cr-rich precipitates, most likely Cr-rich carbides, located predominately at grain boundaries.

Fig. 6d shows ODS-CSM containing nano-oxide particles having a mean size of 8 nm. They are distributed inhomogeneously inside the grains without any preference to grain boundaries.

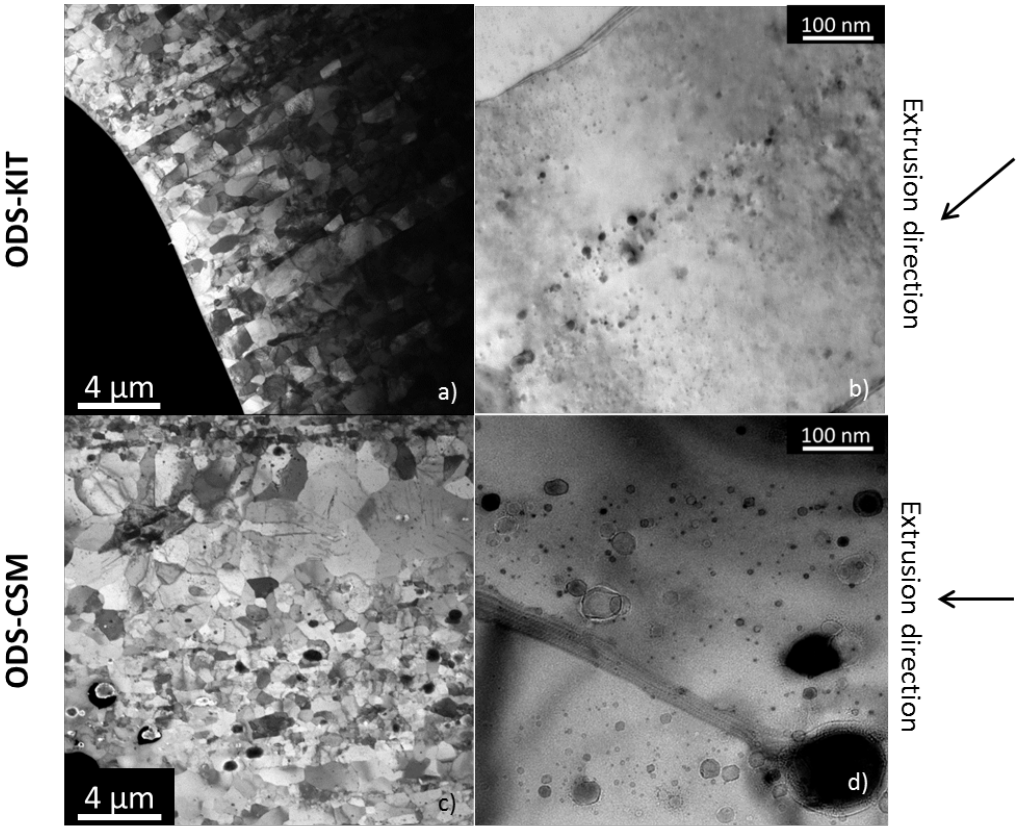

Fig. 6 Low magnification STEM images of a) ODS-KIT and c) ODS-CSM along with bright field TEM images of nano-oxides in b) ODS-KIT and d) ODS-CSM

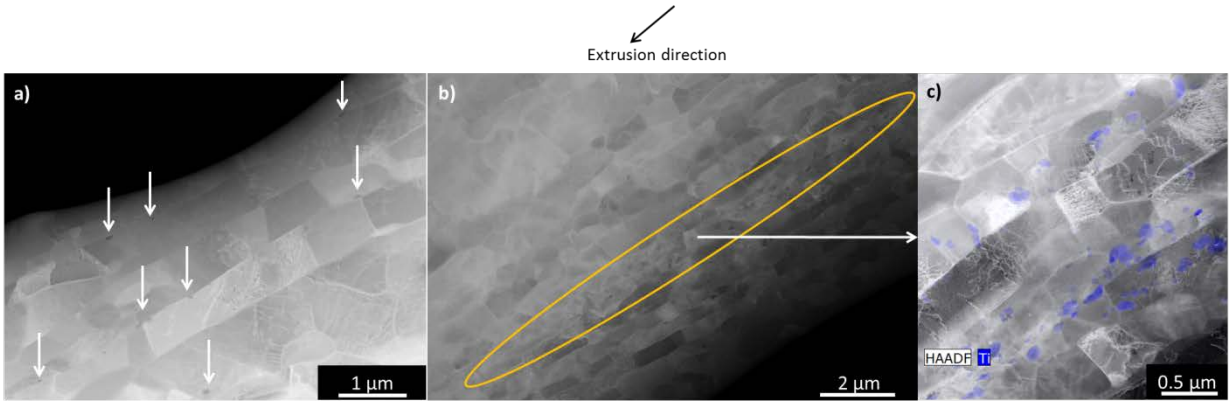

Fig. 7 Low magnification STEM images of ODS-KIT indicating presence of sub-micron particles on a) grain boundaries, b) inside grains aligned parallel to the extrusion direction and c) showing HAADF-STEM image with elemental overlay map of region in b)

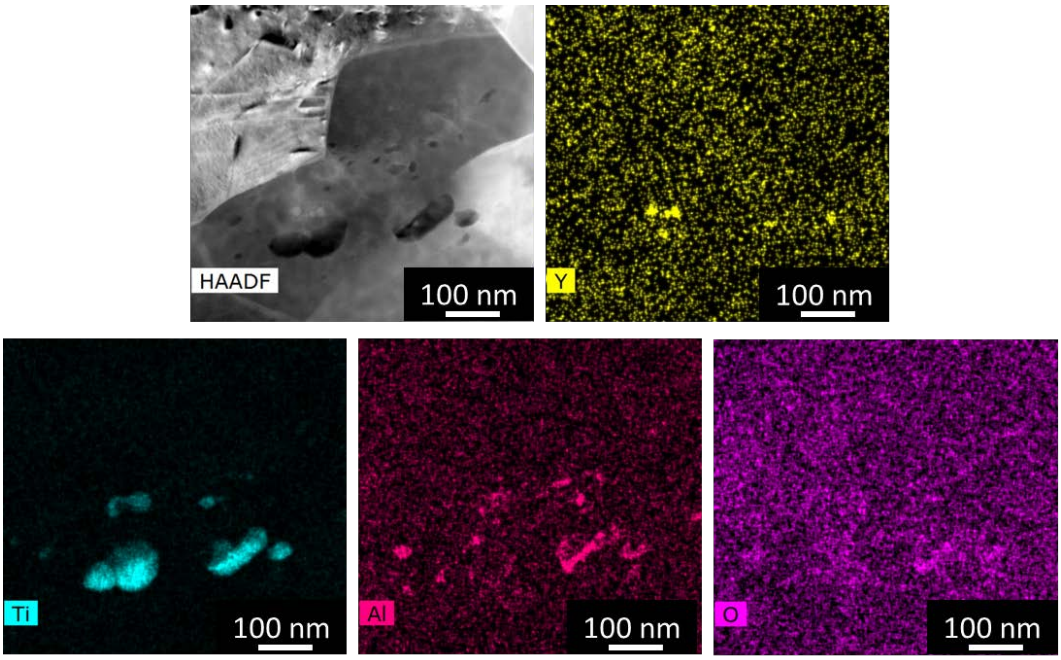

Fig. 8 HAADF-STEM image and elemental maps showing presence of Ti enriched sub-micron particles with traces of Y and Al in ODS-KIT

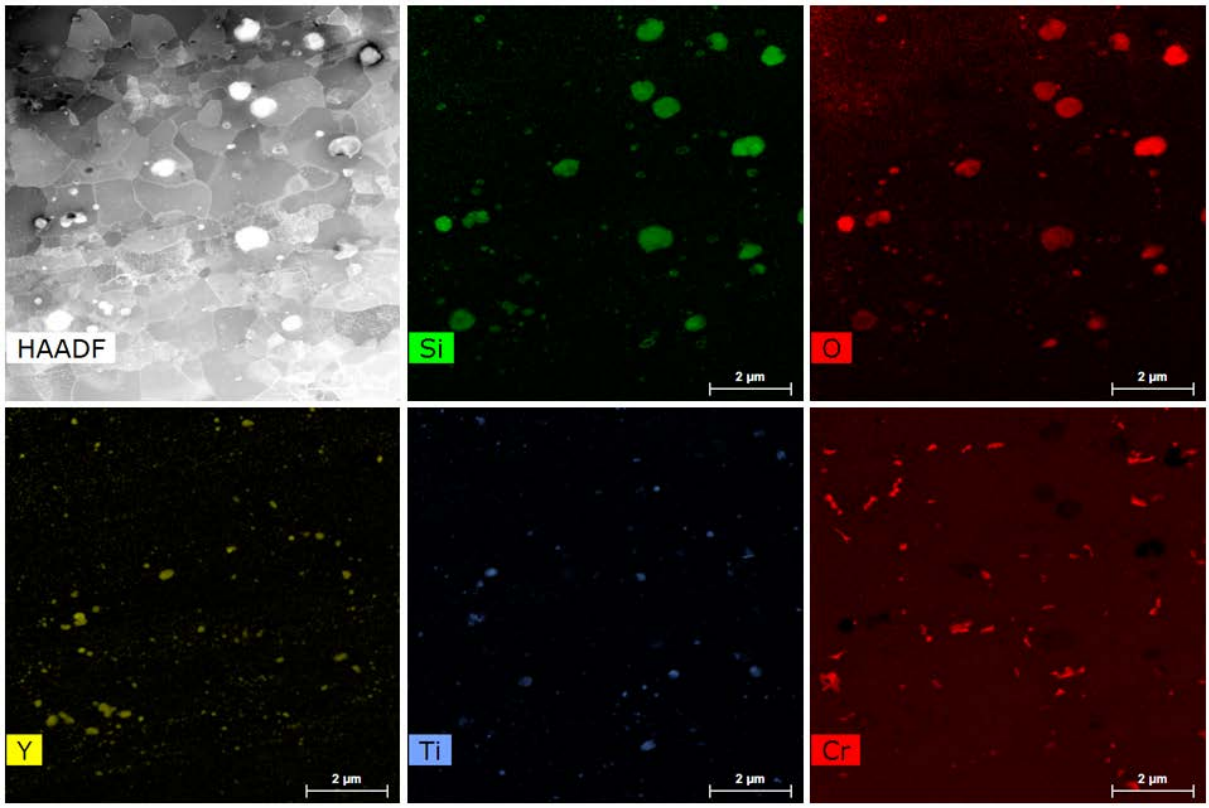

Fig. 9 HAADF-STEM image and elemental maps showing presence of Si and O enriched sub-micron particles along with some smaller Y and Ti particles in ODS-CSM. Cr enrichments can be seen at the grain boundaries.

3.2 Tensile tests

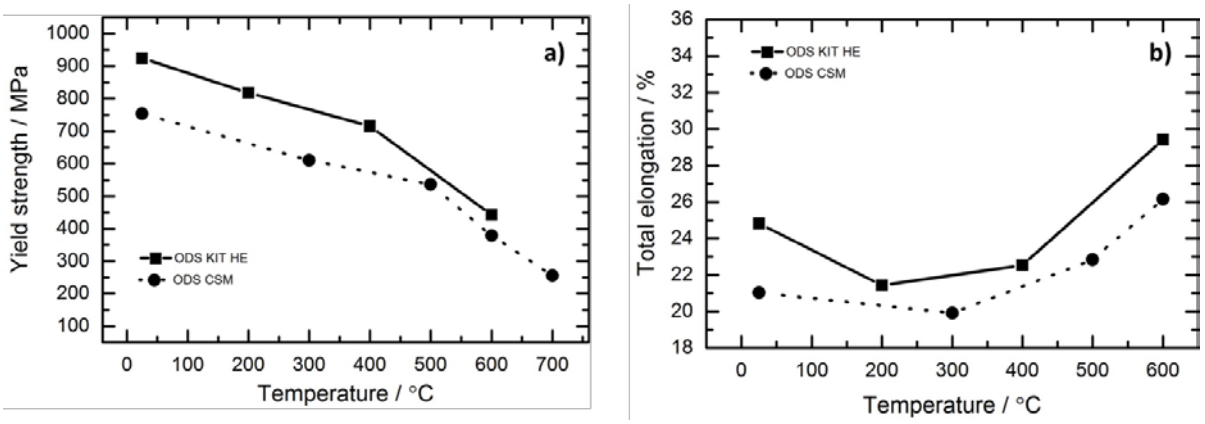

Fig. 10 Yield strength ($R_{p0.2}$) a) and total elongation b) variation with temperature for longitudinal miniature tensile tests in ODS-KIT and ODS-CSM

Fig. 10a shows the yield strength comparison of the two different ODS steels as a function of temperature. Both the materials exhibit a general decrease in yield strength with increase in temperature. ODS-KIT exhibits higher yield strength than ODS-CSM till 400 ˚C. At temperatures higher than 400 ˚C, the yield strength of both the materials drop to have similar values. Fig. 10b shows that ODS-KIT exhibits higher total elongation than ODS-CSM at all temperatures with both materials having the lowest ductility close to 300 ˚C and the highest ductility at 600 ˚C.

3.3 Fracture toughness tests

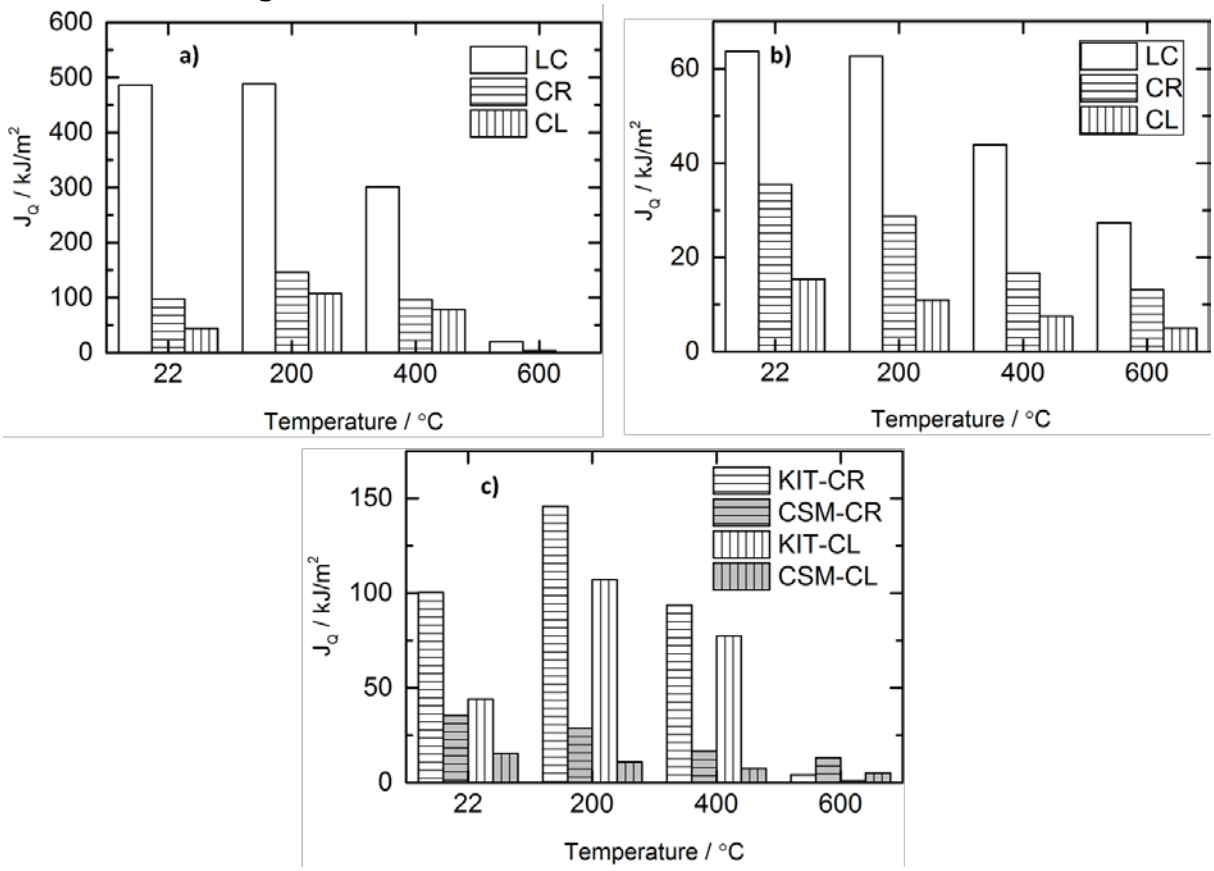

Fig. 11 Fracture toughness J_Q values at various temperatures for the L-C, C-R and C-L oriented specimens in hot extruded a) ODS-KIT, b) ODS-CSM and c) ODS-KIT and ODS-CSM together for the C-R and C-L orientations

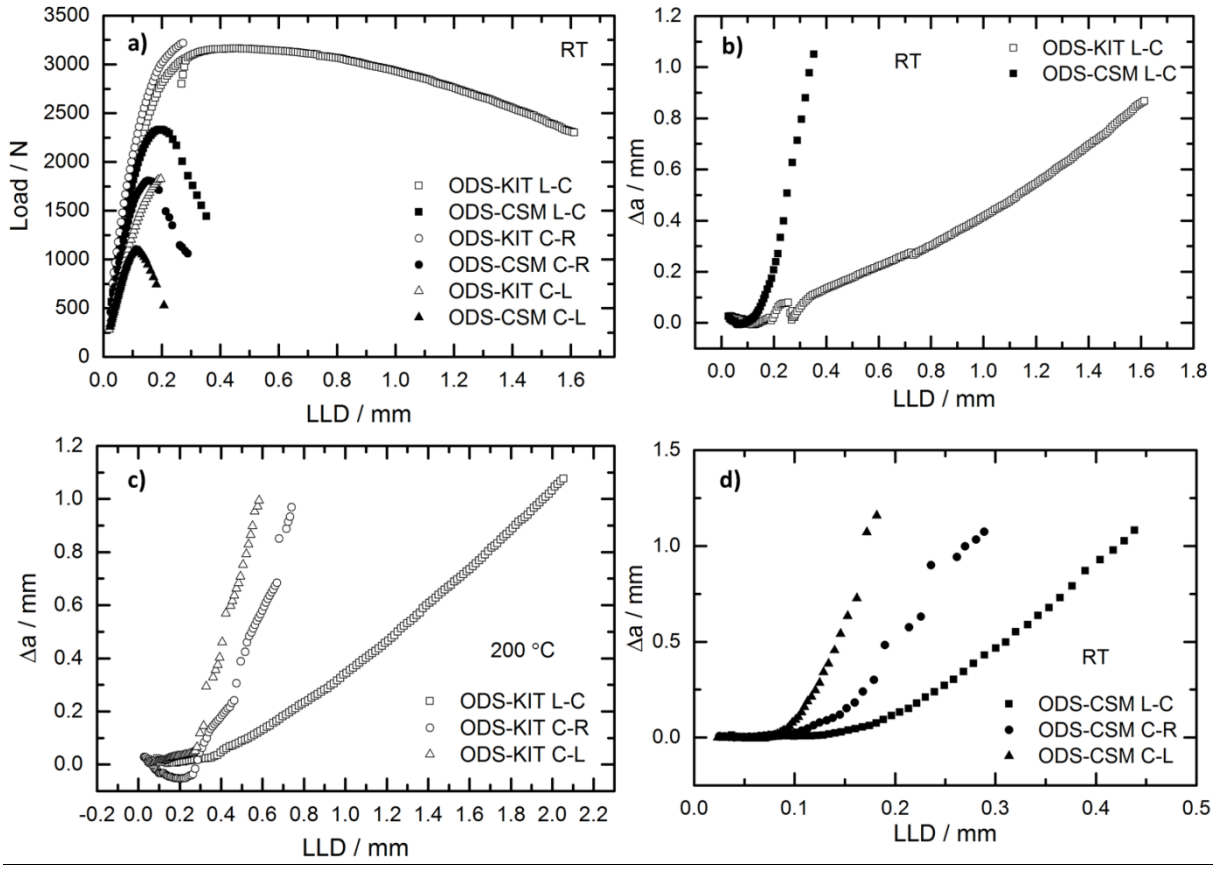

Fig. 12 Curves showing a) load versus load line displacement and b) crack growth (L-C orientation) versus load line displacement for hot extruded ODS-KIT and ODS-CSM at RT, crack growth versus load line displacement curves for c) ODS-KIT at 200 ˚C and d) ODS-CSM at RT

The energy release rate for elastic-plastic material, J integral, is proportional to the fracture toughness of a material. Fig. 11a and b shows the fracture toughness of the L-C, C-R and C-L oriented samples tested for ODS-KIT and ODS-CSM respectively at various temperatures from RT to 600 °C using J_Q values according to ASTM E1820 (determined by the intersection of the J-R curve with 0.2 mm offset line). Fig. 11c shows a comparison of J_Q values in both materials only for the C-R and C-L orientations.

ODS-KIT

Fig. 11a shows that the L-C oriented specimens possess the highest fracture toughness followed by the C-R and C-L orientations. Unstable crack propagation took place in ODS-KIT at RT in the C-R and C-L orientations. Their corresponding fracture toughness values are suffixed with U in Table 5, where all the fracture toughness values at different temperatures are presented. Fig. 11a and Fig. 11b shows that ODS-KIT exhibits an overall superior fracture toughness in all three orientations as compared to ODS-CSM (Table 5) from RT up to 400 ˚C. This high fracture toughness value is well above the acceptable fracture toughness limit of 45 kJ/m^2 (100 MPa√m) as discussed by Byun et al. [5]. The fracture toughness of ODS-KIT steeply decreases between 400 ˚C and 600 ˚C and drops below the acceptable limit.

The load versus displacement graph at RT (Fig. 12a) shows that the maximum load is higher in ODS-KIT than ODS-CSM in all orientations. The load-displacement curves for the C-R and C-L orientations are broken due to unstable crack propagation. The L-C orientation exhibits the largest area under the curve. The crack growth versus load line displacement graph (Fig. 12b) indicates a smaller crack growth for ODS-KIT than for ODS-CSM. The

L-C orientation exhibits the least crack growth as compared to the C-R and C-L orientations for the same load line displacement (Fig. 12c).

ODS-CSM

Fig. 11b shows that the L-C oriented specimens possess the highest fracture toughness in ODS-CSM similar to the case with ODS-KIT. The crack propagation at all temperatures was stable. The fracture toughness of ODS-CSM, although being smaller than ODS-KIT, is nevertheless close to the acceptable limit in the temperature range from RT to 400 ˚C. At 600 ˚C, the drop in fracture toughness is not so steep in ODS-CSM as compared to ODS-KIT and settles just below the acceptable limit (Table 5).

The maximum load and area under the curve for ODS-CSM is the highest in the L-C orientation as seen from the load-displacement curve (Fig. 12a) but is lower than that of ODS-KIT. The crack growth versus load line displacement graph (Fig. 12b) indicates larger crack growth for ODS-CSM than ODS-KIT for the same load line displacement. Fig. 12d shows that the L-C orientation has the least crack growth as compared to the C-R and C-L orientations for the same load line displacement similar to the trend observed in ODS-KIT.

Table 5 Fracture toughness (J_Q) values for ODS-KIT and ODS-CSM at various temperatures

Temperature °C	KIT J_Q (L-C) kJ/m^2	KIT J_Q (C-R) kJ/m^2	KIT J_Q (C-L) kJ/m^2	CSM J_Q (L-C) kJ/m^2	CSM J_Q (C-R) kJ/m^2	CSM J_Q (C-L) kJ/m^2
22	486.27	97.26U	44.07U	63.68	35.48	15.31
200	488.52	146.17	107.54	62.64	28.72	10.87
400	300.73	95.6	78.06	43.87	16.7	7.5
600	19.69	4.04	0.95	27.35	13.13	5

3.4 Fracture surfaces

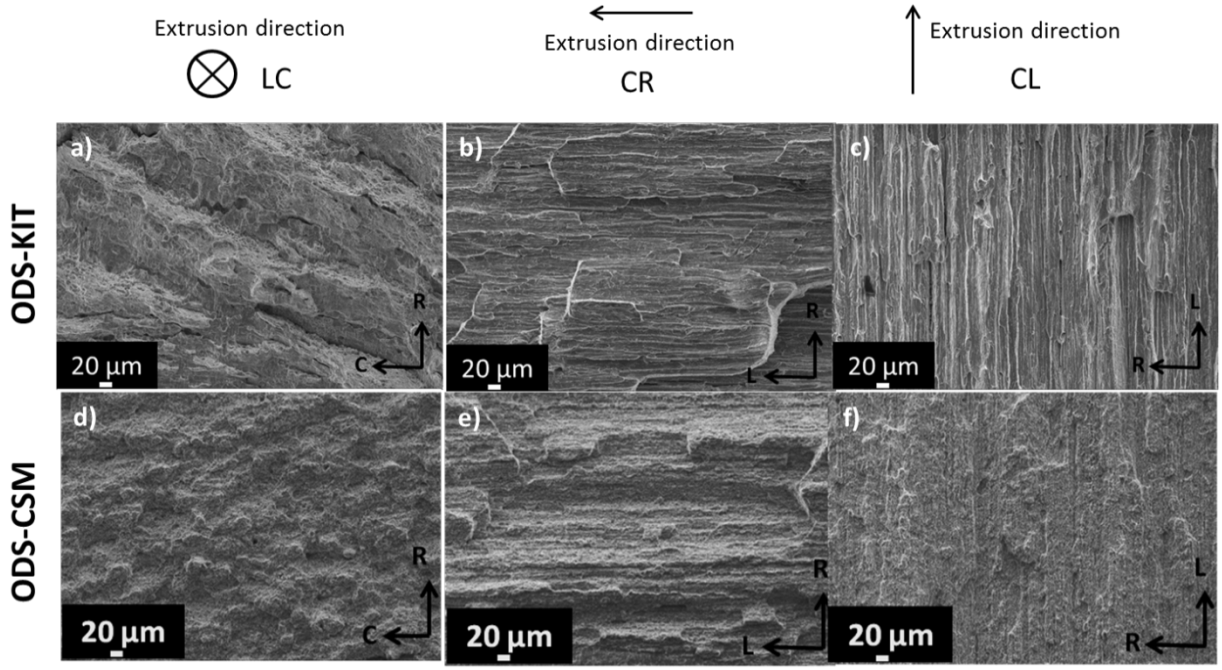

Fig. 13 Low magnification SEM images of fractures surfaces at RT in different orientations of (a-c) ODS-KIT and (d-f) ODS-CSM

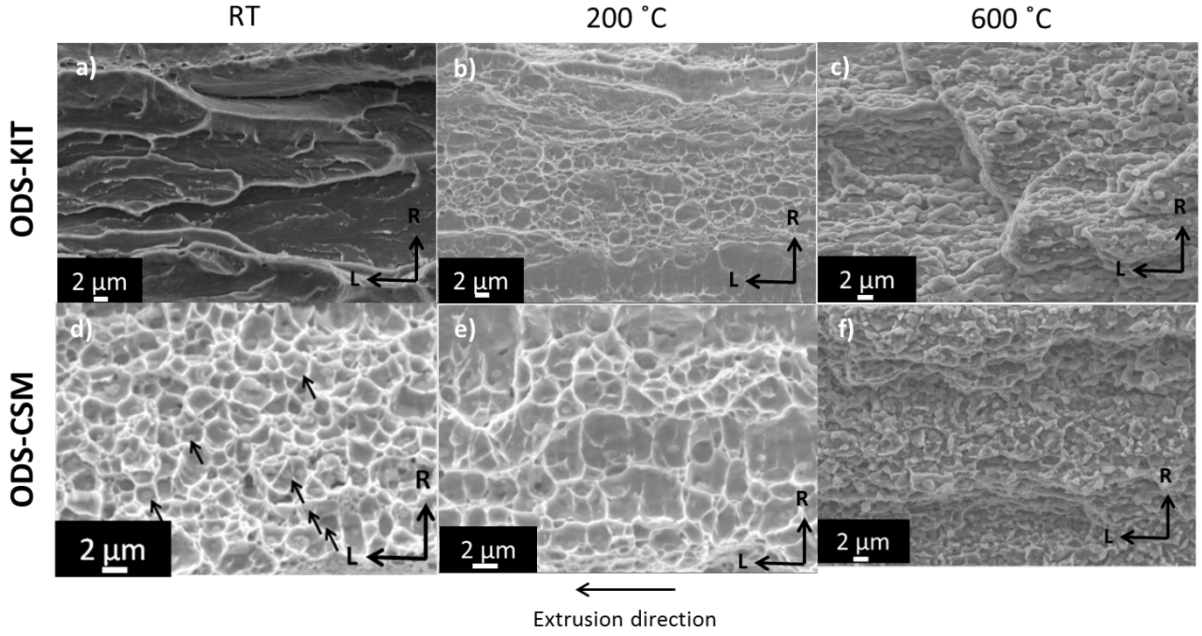

Fig. 14 High magnification SEM images of fracture surfaces in the C-R orientation at different temperatures of (a-c) ODS-KIT and (d-f) ODS-CSM

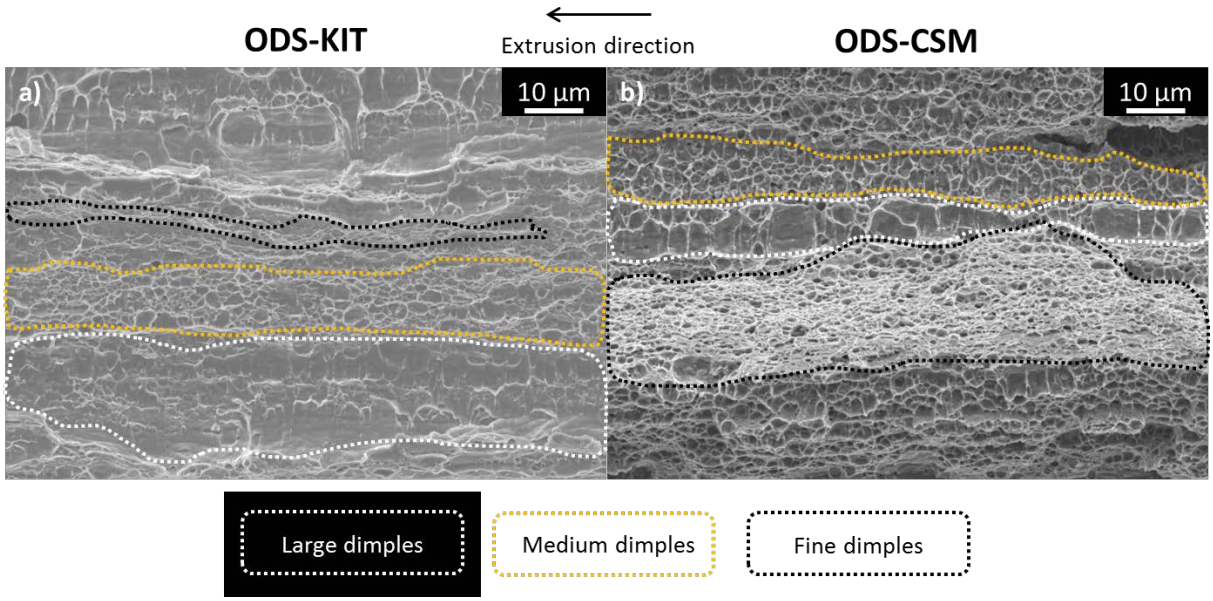

Fig. 15 Low magnification SEM fracture surface pictures of a) ODS-KIT at 200 ˚C and b) ODS-CSM at RT in the C-R orientation. Three different zones of dimples are indicated which depend on the size and density of void-inducing particles

ODS-KIT

Fig. 13a-c shows the low magnification SEM images of the fracture surfaces for all orientations tested at RT. Fracture morphology with features parallel to the extrusion direction are observed. Predominant cleavage fracture with occasional ductile tearing is observed in the C-R and C-L orientations similar to the work in reference [17] while the fracture in the L-C orientation exhibits flat dimples. Fig. 14a-c shows the temperature effect on the fracture behaviour in the C-R orientation. Fig. 14a shows steps and ridges characteristic of cleavage fracture at RT. Fig. 14b shows dimples characteristic of ductile fracture at 200 ˚C and Fig. 14c shows particle like nano-features characteristic of inter-granular fracture at 600 ˚C. Such nano features on the fracture surface were also observed in other works [4,18–20]. Fig. 15a shows a low magnification picture of ODS-KIT at 200 ˚C in the C-R orientation. In the ductile regime (T ≥ 200 ˚C), the fracture surface consists of flat regions of large dimples, medium dimples (mean size 3.2 µm) and fine dimples (mean size 0.7 µm). It is interesting to note that secondary cracking or delamination, which was observed in many ODS steels [4,10,11,17,21,22], are not observed on the fracture surfaces. However, secondary cracking and related issues will not be discussed here as it is beyond the scope of this paper.

ODS-CSM

Fig. 13d-f shows the fracture morphology with features parallel to the extrusion direction for ODS-CSM. Cleavage fracture is absent in all the three orientations. Fig. 14d shows dimples which are characteristic of ductile fracture at RT. Fig. 14e also shows dimples indicating ductile fracture at 200 ˚C, and Fig. 14f shows particle like nano-features indicating failure through inter-granular fracture at 600 ˚C. In the ductile regime (RT), similar regions as in ODS-KIT are observed; containing fine dimples (mean size 0.7 µm) and medium dimples (mean size 1.1 µm) are observed (Fig. 15b). The large dimples in ODS-CSM however, are not as large as in ODS-KIT. Like for ODS-KIT, no secondary cracking is observed on the fracture surfaces.

4 Discussion

4.1 Factors affecting fracture toughness

ODS-KIT specimens at RT in the C-R and C-L orientations fail through cleavage fracture (Fig. 13b & c and Fig. 14a) as a consequence of its higher ductile to brittle transition temperature (DBTT) than ODS-CSM. Impact testing to determine DBTT could not be performed since the required amount of material was not available. Small punch tests (SPT) were used alternatively to investigate the DBTT and a comparative study will be published in the future.

The DBTT of ODS-KIT is expected to be higher than that of ODS-CSM due to absence of Ni and higher average coarse grain size (Table 3) [23]. Nevertheless, it is observed that ODS-KIT consistently exhibits a higher fracture toughness than ODS-CSM (Fig. 11a and b) in all three orientations from RT to 400 ˚C. In fact, these fracture toughness values are even higher than other ODS steels investigated before [5]. The fracture toughness drops drastically at high temperatures (T > 600 ˚C) due to inter-granular fracture. The reasons for this loss of fracture toughness are linked to weakening of grain boundaries due to segregation of O, N and C at grain boundaries [24], dislocation pileup at grain boundaries [18,19,25], Ti and O rich stringers at prior particle boundaries [26] and shallow plastic deformed zone formation [4]. More information about high temperature deformation mechanisms were reported elsewhere [19,27,28]. Cr segregations at the grain boundaries of ODS-CSM also possibly act as barriers to grain boundary movement thus making grain boundary sliding difficult at high temperatures. The degradation of fracture toughness from 400 ˚C to 600 ˚C is therefore lower for ODS-CSM than ODS-KIT. Similar effect was observed in reference [29].

It is assumed that ductile fracture is dominant for all orientations in both materials from RT to 400 ˚C. In case of ductile fracture, according to the stress-modified critical strain criteria, fracture in an isotropic material occurs when the local equivalent plastic strain exceeds a critical fracture strain $\bar{\epsilon}_f^*$ over a characteristic distance l [30–32]. The fracture toughness is proportional to the flow stress, the critical fracture strain and the inter-particle spacing (Eq. 1). In Eq. 1, the product of critical fracture strain and characteristic length is an indication of the local ductility of the material. Ashby's work suggested that the de-cohesion strain between the particle and the matrix is dependent on the work of adhesion between the particle and the matrix and other factors as shown in Eq. 2 [32–34]. In this context, it is assumed that the void initiating particles are of equal size, are equally spaced and pre-existing dislocation density and tangling are neglected.

Assuming the critical fracture strain ($\bar{\epsilon}_f^*$) to be equal to the de-cohesion strain (ϵ) between the particle and the matrix for the initiation of ductile fracture, J_{IC} is written in terms of microstructural parameters (W, l and d), flow stress, shear stress and burgers vector (Eq. 3).

$$J_{IC} \sim \sigma_0 * \bar{\epsilon}_f^* * l \quad (1)$$

$$\epsilon = \frac{2 * W * l}{G * b * d} \quad (2)$$

$$J_{IC} \sim \sigma_0 * \frac{2 * W * l^2}{G * b * d} \quad (3)$$

where,

σ_0= Flow stress

$\bar{\epsilon}_f^*$ = Critical fracture strain

ϵ = De-cohesion strain between particle and the matrix

l = Mean void initiating particle spacing

W = Work of adhesion or particle – matrix bond strength

G = Shear modulus

d = Size of the particle

b = Burgers vector

In hot extruded materials, anisotropy plays a huge role which however, is not incorporated in Eq. 3 as it was developed for an isotropic material. The following parameters affect the fracture toughness in the ductile regime, few of them possessing anisotropy:

Flow stress (σ_0)

The yield and ultimate tensile strength of ODS-KIT is higher than that of ODS-CSM (Fig. 10) in the longitudinal direction which contributes towards higher fracture toughness in ductile fracture (Eq. 1). It was reported in other works that the flow stress in the transverse orientation is similar to the one in longitudinal orientation[8,35]. The flow stress depends on how effective the nano-particles are in obstructing dislocations, the size and the inter-particle spacing of nano-particles being important parameters. The fact that ODS-KIT was produced by Fe_3Y precursor while ODS-CSM was produced by Y_2O_3 precursor can have an effect on the nano-particles and their ability to obstruct dislocations, but this is not confirmed through experiments. Similar precursor Fe_2Y however, used in other works, led to formation of nano-particles similar to the ones obtained from Y_2O_3 precursor [36] and resulted in similar yield strength as from Y_2O_3 precursor at all temperatures [37].

Kim et al. [29] observed the nano-particles to be present on grain boundaries. However, in this work, the nano-particles of both materials have no preferential location and are distributed inhomogeneously in certain high density regions (Fig. 6b and d). The inter-particle spacing in the homogeneous regions of both materials is similar (inter-particle spacing: 10 nm and volume fraction: 0.148) however, ODS-KIT has slightly smaller nano particle size (average size: 3 nm) than ODS-CSM (average size: 8 nm). Therefore the strengthening induced by nano-clusters is more pronounced in ODS-KIT. Strengthening is also dependent on the grain size through the Hall-Petch relation [29]. The fine grains in both materials have a similar size (0.65 µm) however the coarse grains of ODS-KIT (4.7 µm) are larger than coarse grains of ODS-CSM (2.1 µm). The contribution from Hall-Petch strengthening to flow stress is therefore more pronounced in ODS-CSM than in ODS-KIT. However, other factors such as dislocation forest strengthening which depends on the initial severe plastic deformation and grain matrix hardening [29] probably have a greater contribution resulting in higher flow stress in ODS-KIT.

Shear Modulus (G)

The shear modulus is similar for both materials owing to their similar compositions. However, due to the <110> texture parallel to the extrusion direction (L), the shear modulus in the extrusion (L) direction is different from the radial (R) and the circumferential (C) direction (considering a transversely isotropic material). Walpole et al. proved that minimum shear modulus in a cubic crystal is achieved in the <110> direction [38]. This minimum shear modu-

lus is calculated to be 48 GPa using compliance constants of bcc iron [39]. The other directions R and C contain a mixture of all crystal orientations with no dominant texture and hence can be considered isotropic. The isotropic shear modulus is calculated to be 73 GPa using compliance constants [40]. The ratio of minimum shear stress in L direction to isotropic shear stress in R or C direction is calculated to be 0.66.

It was also reported in another work that the <110> direction (which was parallel to the extrusion direction) exhibits higher void nucleation and growth in ductile fracture as compared to other directions [41].

Void initiating particles (l and d)

Chaouadi et al. [42] reported that stress-strain incompatibility between hard nano-oxide particles and soft iron matrix promotes void nucleation, growth and coalescence. However, it was observed from other studies that void initiation, growth and coalescence is preferred on sub-micron particles rather than on nano-oxide particles [32,43–45]. Byun et al. [4,46] found that fracture processes occurring on the nano-scale have limited influence on fracture toughness and that meso- and macroscopic failure mechanisms are the main reasons for failure. Also, due to the resolution limit of SEM, no evidence was found for the role of nano-oxides in dimple formation. Similar conclusions were made in reference [46].

Therefore, sub-micron particles are given the main focus in the present work for the ductile fracture mechanisms which occurred between RT and 400 ˚C. The larger the inter-particle spacing (l) is and the smaller the particle size (d), the higher is the fracture toughness (Eq. 3). These two parameters can vary from material to material and also within different regions of one material due to inhomogeneity.

The fracture surfaces exhibit dimples in the ductile regime for both materials. The width and height of a dimple depends on the size and the density of void initiating particles. When the particles are densely packed, the dimples are finer as a growing dimple meets its neighbour at short distances and gets arrested. When the particles are located far away from each other, the dimples can grow and reach larger dimensions before getting arrested by its neighbouring dimple. The pronounced existence of large and medium sized dimple regions in ODS-KIT (in the ductile regime) suggest a higher number of low density sub-micron particle regions than in ODS-CSM (Fig. 15).

This is confirmed by TEM images where thin bands of Ti enriched sub-micron particles with high number density and thick zones of sub-micron particles with low number density are observed in ODS-KIT (Fig. 7b). It is seen that the Si and O enriched sub-micron particles in ODS-CSM are present in high density zones which are, elongated parallel to the extrusion direction (Fig. 6c). These sub-micron particles are possibly formed due to the high Si content in the matrix and contaminations picked up during the manufacturing process. It is fair to assume that improper milling led to inhomogeneous sub-micron particle distribution. The effect of such arrangement of sub-micron particles on fracture toughness will be discussed in further sections.

Particle-matrix bond strength (W)

The particle-matrix bond strength depends on chemical composition of the sub-micron particle and the matrix. The higher this bond strength is, the higher is the fracture toughness. It is fair to assume that the Ti enriched sub-micron particles in ODS-KIT and Si, O enriched sub-

micron particles in ODS-CSM have different values of W. This affects the fracture toughness differently. More details are discussed in section 4.3.

Grain morphology

In an isotropic material, the grain sizes and shapes are similar. However, in both ODS-KIT and ODS-CSM, bimodal grains elongated parallel to the extrusion direction are observed. The reason for bimodality in grain structure is the inhomogeneous dislocation density formed after mechanical alloying which results in subsequent inhomogeneous recrystallization [47] during hot extrusion. This affects fracture toughness and is not taken into account by Eq. 3. In the next section we discuss in detail, how grain morphology affects fracture toughness.

4.2 Effect of microstructural anisotropy on fracture toughness

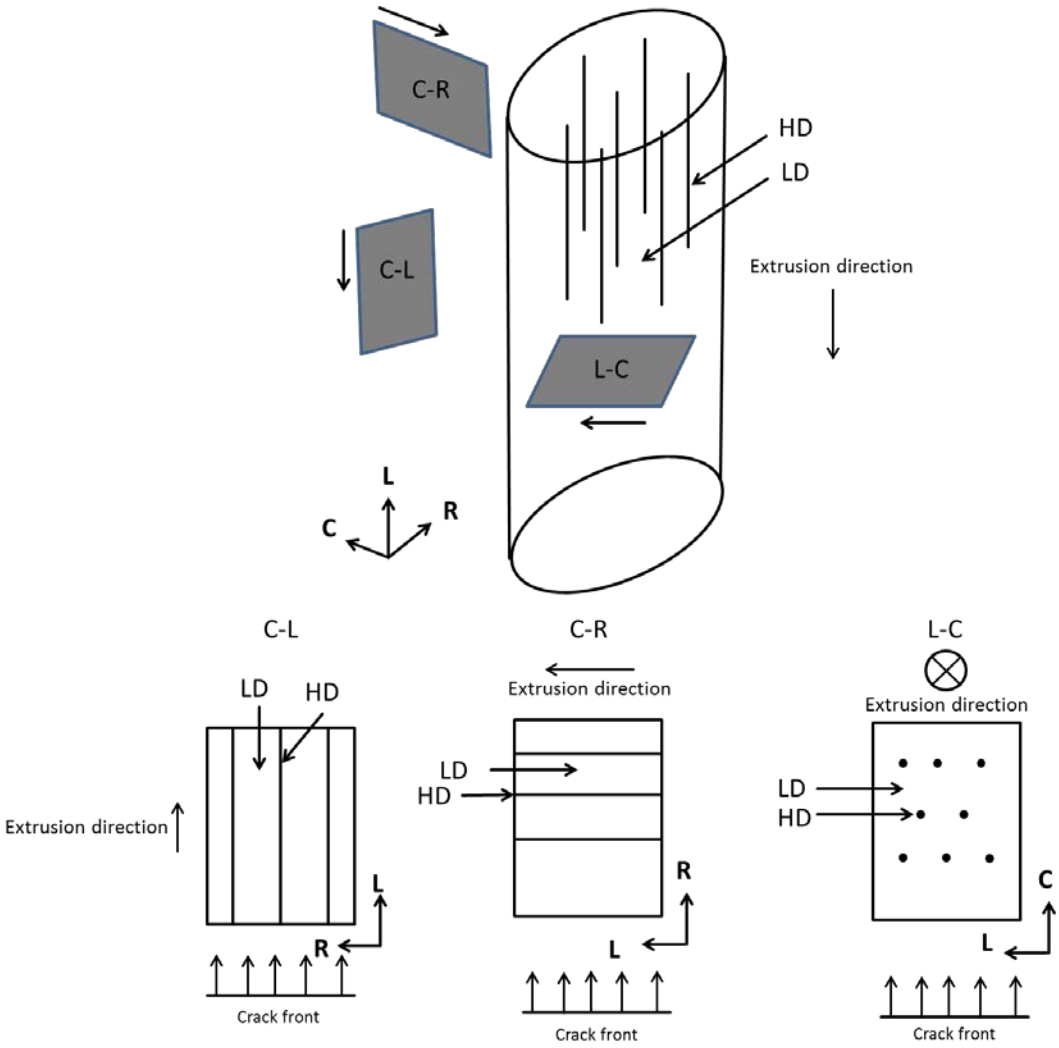

Fig. 16 Schematic showing propagating primary crack planes in different orientations and their relation with high density sub-micron particle region (HD) and low density sub-micron particle region (LD) aligned parallel to extrusion direction

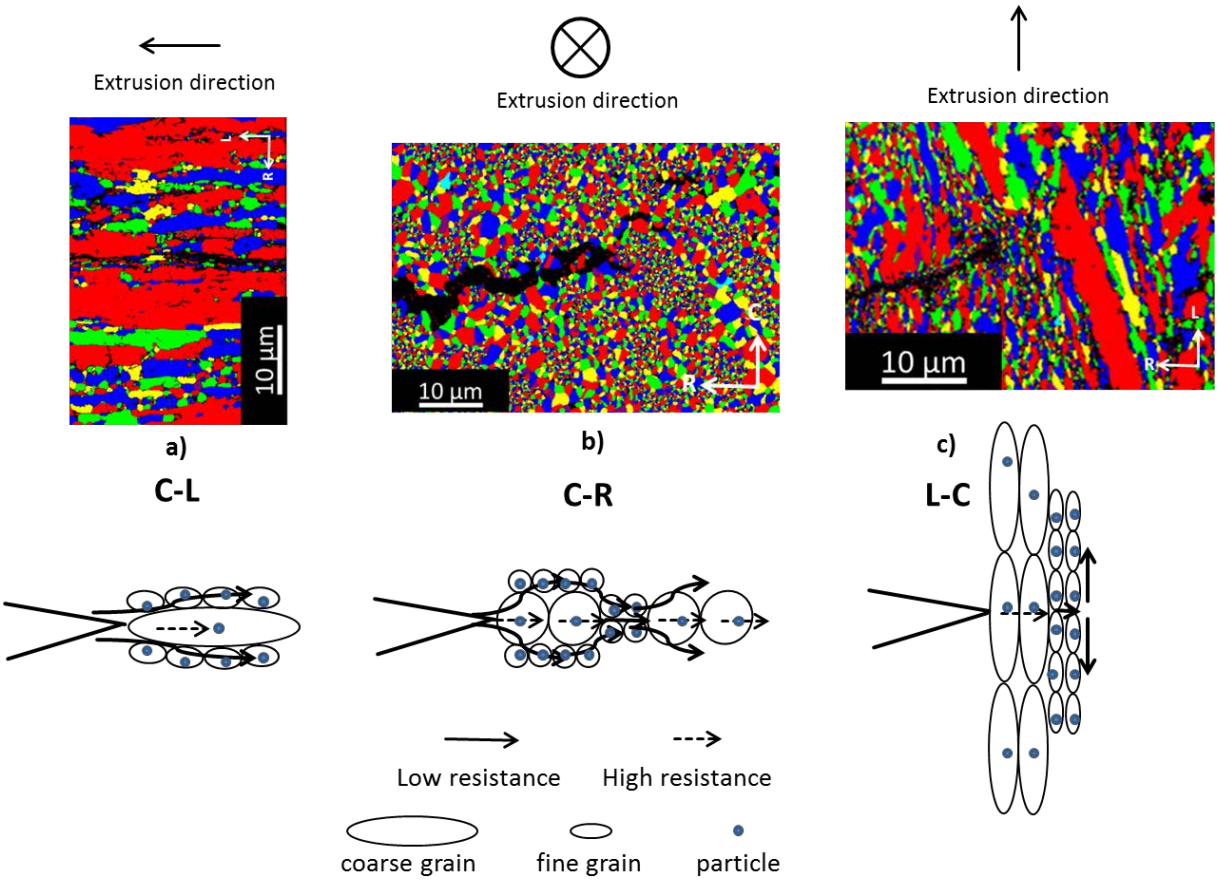

Fig. 17 Schematic showing side view of crack propagation in all the three orientations along with EBSD grain distribution maps supporting them

Crack propagation or crack growth is a measure of fracture toughness. The lesser the crack propagation is at a given driving force, the higher is the fracture toughness. Smaller crack propagation in the L-C orientation (Fig. 12c and d) as compared with the C-R and C-L orientation results in higher fracture toughness of the L-C orientation in both the materials. Similar kind of fracture toughness anisotropy was also reported in other works [7–11].

To understand the effect of sub-micron particle distribution anisotropy on fracture toughness, the crack propagation planes in all the three orientations L-C, C-R and C-L are visualized in relation to the aligned sub-micron particles in Fig. 16. For simplicity, only one material (ODS-KIT) is analysed for anisotropy. A similar analysis can be performed for ODS-CSM. The crack propagates through the low density (LD) and the high density (HD) particle regions.

Using Eq. 3 for the ductile fracture of ODS-KIT at 200 ˚C, one can find the ratios of fracture toughness in different orientations (C-R/C-L and L-C/C-L) and correlate it with ratios of microstructural features (l and d), shear stress and flow stress:

$$\frac{J_{IC}^{CR}}{J_{IC}^{CL}} = \frac{\sigma_0^{CR}}{\sigma_0^{CL}} * \frac{G_{CL}}{G_{CR}} * \frac{l_{CR}^2}{l_{CL}^2} * \frac{d_{CL}}{d_{CR}} \text{ and } \frac{J_{IC}^{LC}}{J_{IC}^{CL}} = \frac{\sigma_0^{LC}}{\sigma_0^{CL}} * \frac{G_{CL}}{G_{LC}} * \frac{l_{LC}^2}{l_{CL}^2} * \frac{d_{CL}}{d_{LC}} \quad (4)$$

C-L orientation

It is seen that the crack propagates through ultra-fine grains (UFGs) which are aligned in zones parallel to the extrusion direction. Similar results were reported in reference [22] where it was discussed, how UFGs provide lower resistance to crack propagation as compared to coarse grains. In the case of ODS-KIT, there is a possibility of crack deviation towards other adjacently lying ultra-fine grained zones. Fig. 17a shows an EBSD grain distribution map of ODS-KIT containing zones of elongated coarse and fine grains along with the side view of the propagating crack in the C-L orientation. Minimal crack deviation (like shown in schematic) is observed due to the alignment of the UFGs in the same direction as the crack propagation. The energy dissipation due to obstruction by coarse grains is small.

Apart from grains, the particle anisotropy also affects fracture toughness. The crack propagates through the high density particle region and low density particle region in a parallel combination. The sub-micron particles are aligned parallel to the extrusion direction which is also the direction of crack propagation (Fig. 16). The resistance to crack propagation is higher in low particle density region than in high particle density region. Effective values of inter-particle spacing and particle size for the propagating crack plane are calculated using a parallel combination analogous to a mechanical system with parallel springs (Eq. 5 and 6) and are presented in Table 6. The fractions of low density and high density particle region ($p_{HD}$and p_{LD}) encountered by the propagating crack planes are calculated using thicknesses of LD and HD zones (Table 6).

$$l_{CL} = \ l_{eff} = p_{HD} * l_{HD} + p_{LD} * l_{LD} \tag{5}$$

$$d_{CL} = \ d_{eff} = p_{HD} * d_{HD} + p_{LD} * d_{LD} \tag{6}$$

where,

l_{eff} = Effective inter-particle spacing in the C-L orientation

d_{eff} = Effective particle size in the C-L orientation

l_{HD} = Inter-particle spacing in high density region

l_{LD} = Inter-particle spacing in low density region

d_{HD} = Particle size in high density region

d_{LD} = Particle size in low density region

p_{HD} = Fraction of high density particle zone encountered by the crack front

p_{LD} = Fraction of low density particle zone encountered by the crack front

Table 6 Microstructural parameters of inter-particle spacing and particle size in the C-L orientation

Material	p_{HD}	p_{LD}	${l_{LD}}^2$	d_{LD}	${l_{HD}}^2$	d_{HD}	l_{eff}^2	d_{eff}
ODS-KIT	0.05	0.95	0.76	0.06	0.048	0.06	0.701	0.06
ODS-CSM	0.42	0.58	2.72	0.09	8.58	0.47	4.78	0.25

Table 7 Microstructural parameters of inter-particle spacing and particle size in LD regions for the C-R and L-C orientations

Material	${l_{LD}}^2$	d_{LD}
ODS-KIT	0.76	0.06

C-R orientation

The possibility of crack deviation along UFGs exists for ODS-KIT C-R oriented specimen in a similar way as shown in an example involving ODS-CSM (Fig. 17b). The C-R fracture surfaces exhibit a wavy macro surface morphology (Fig. 13) confirming crack deviation. However, the energy dissipation is still small as the crack can find a path of least resistance to propagate.

In the C-R orientation, the crack plane propagates through the high density and low density particle regions one after the other as the direction of crack propagation is perpendicular to the extrusion direction (Fig. 16). The J_{IC} value depends on the regions through which the crack propagates until a crack extension of 0.2 mm is reached. In case of ODS-KIT, the high density particle regions are very thin. For simplification, it is therefore reasonable to assume that the crack travels predominantly through the low particle density region. Consequently, the inter-particle spacing and size of the particles can be associated with the LD region (Table 7).

L-C orientation

During propagation the crack is blunted while passing through the perpendicularly elongated coarse grains and cannot access any low resistance path by crack deviation. This can be seen in Fig. 17c where the side view of ODS-KIT crack propagation for the L-C oriented sample is shown. The energy dissipation through crack propagation is the highest in this orientation.

The crack has to cut through both the high and the low density particle regions (lying parallel to the extrusion direction) towards a direction perpendicular to the extrusion direction (Fig. 16). A similar simplification assuming crack propagation only through low density particle region can also be made for the L-C orientation as it was done for the C-R orientation (Table 7).

Analysis

The ratios of contributing factors for fracture toughness are obtained using Eq. 4 and are presented in Table 8. Note that the flow stress ratio of the materials remain similar from RT to 400 ˚C in different orientations [8,35]. Crystallographic texture of <110> parallel to the extrusion direction results in different shear moduli in different directions as discussed in the previous section. This means that the shear modulus of the L-C orientation (towards extrusion direction) is the lowest and its ratio with the shear modulus of the C-L orientation is close to 1.5. The C-R and C-L orientations are considered to be equally isotropic and hence their shear moduli are assumed to be equal.

Table 8 Ratios of contributing factors to ODS-KIT fracture toughness in the C-R and L-C with respect to the C-L orientation at 200 ˚C

Orientation Ratio	$J_{IC}\ Ratio$	$\sigma_0\ Ratio$	G Ratio	$l^2\ Ratio$	$d\ Ratio$
CR/CL	1.36	≈1	1	1.08	1
LC/CL	4.54	≈1	≈1.5	1.08	1

It is observed that the inter-particle spacing and particle size do not significantly contribute to the increase in fracture toughness when comparing the C-R and L-C orientation with the C-L orientation (Table 8). The low shear modulus in the L-C orientation contributes to the increase in fracture toughness ratio. However, the increase is not big enough to compensate for the actual increase in the fracture toughness observed during the experiment ($\frac{J_{IC}^{LC}}{J_{IC}^{CL}} = 4.54$). This is due to the fact that Eq. 3 was derived for isotropic materials where the particles are of equal size, have equal spacing and have isotropic grains.

ODS-KIT, however, contains various kinds of anisotropic features as discussed earlier. The grain morphology anisotropy leads to crack tip blunting [22], which plays a major role in increasing the fracture toughness of certain orientations. Its contribution however, is missing from Eq. 3 and Eq. 4. The L-C orientation promotes the highest crack blunting through perpendicularly elongated coarse grains and hence has the highest fracture toughness of all orientations. The contribution from crack blunting is minimal in the C-R and C-L orientations as the crack can deviate and follow the path of least resistance (through adjacent lying high density particle regions or ultra-fine grained zones).

4.3 Effect of void inducing particle properties on fracture toughness

In the last section, microstructural anisotropic effects of an individual material (ODS-KIT) were discussed for different orientations at 200 ˚C. In this section, two different hot extruded materials, ODS-KIT and ODS-CSM are compared in the C-L orientation with respect to all the factors affecting the fracture toughness.

Larger crack propagation (Fig. 12c and d) leads to lower fracture toughness in ODS-CSM as compared to ODS-KIT. At 200 ˚C, Eq. 3 for ductile fracture can be used for both materials to separate the relative contributions of flow stress, inter-particle spacing, size of the sub-micron particle and interfacial bond strength between sub-micron particle and matrix. Eq. 7 shows the separated ratios. The burgers vector is assumed to be the same for both materials as both materials have BCC Fe matrix. As both materials exhibit a <110> texture towards extrusion direction, it is reasonable to assume that for the C-L orientation, the shear moduli of both materials are similar. The contribution from crack blunting (explained in the previous section), is also assumed to be similar for both materials in the C-L orientation.

$$\frac{J_{IC}^{KIT}}{J_{IC}^{CSM}} = \frac{\sigma_0^{KIT}}{\sigma_0^{CSM}} * \frac{l_{KIT}^2}{l_{CSM}^2} * \frac{d_{CSM}}{d_{KIT}} * \frac{W_{KIT}}{W_{CSM}} \tag{7}$$

Table 9 Relative contributions of various factors towards fracture toughness at 200 ˚C

Orientation	$\frac{J_{IC}^{KIT}}{J_{IC}^{CSM}}$	$\frac{\sigma_0^{KIT}}{\sigma_0^{CSM}}$	$\frac{l_{KIT}^2}{l_{CSM}^2}$	$\frac{d_{CSM}}{d_{KIT}}$	$\frac{W_{KIT}}{W_{CSM}}$
C-L	9.89	1.14	0.15	4.2	13.8

The flow stress ratio between ODS-KIT and ODS-CSM at 200 ˚C amounts to a value of only 1.14. Therefore the superior fracture toughness in ODS-KIT as compared to ODS-CSM must be predominantly due to particle properties such as the inter-particle spacing (l), size of the particle (d) and interfacial strength between particle and matrix (W). The effective inter-particle spacing and effective mean size in the C-L orientation are calculated using Eq. 5 and Eq. 6, respectively (Table 9). The ratio of inter-particle spacing lowers the fracture toughness ratio because the inter-particle spacing of ODS-CSM is larger than that of ODS-KIT (Table 4). The smaller sub-micron particle size of ODS-KIT however, proves to be beneficial for the fracture toughness ratio (Table 9). These contributions however, still cannot explain the high value of experimental fracture toughness of ODS-KIT as compared to ODS-CSM ($\frac{J_{IC}^{KIT}}{J_{IC}^{CSM}} = 9.89$). It can only be explained if the interfacial particle-matrix strength of ODS-KIT is higher than ODS-CSM. This ratio is obtained using known ratios (Table 9) of fracture toughness, flow stress, inter-particle spacing and particle size in Eq. 7 and is solved for the interfacial particle-matrix strength ratio.

The above analysis suggests that the highest contribution to fracture toughness in ODS-KIT comes from the interfacial particle-matrix strength. It can also be concluded that the interfacial particle-matrix strength of Ti particles with ODS-KIT matrix is higher than Si and O particles with ODS-CSM matrix. This should however, be confirmed with direct experimental or simulation based investigations in the future. The Cr enrichments at grain boundaries may have additionally contributed to the lower fracture toughness in ODS-CSM.

5 Conclusions

- Fracture toughness of ODS-KIT is higher than ODS-CSM in the temperature range from RT to 400 ˚C due to microstructural properties such as higher particle-matrix interfacial strength and smaller sub-micron particles than ODS-CSM.
- In both the materials, the fracture toughness is highest in the L-C orientation followed by the C-R and C-L orientations. Crack blunting due to anisotropy in grain morphology contributes to the maximum fracture toughness in the L-C orientation. Crack deviation through low resistance paths in the C-R and C-L orientations lead to lesser energy dissipation as compared to the L-C orientation which experiences crack blunting.
- Crystallographic <110> texture towards extrusion direction affects the shear modulus and the fracture toughness. However it is not, the dominant factor affecting the fracture toughness.
- Anisotropy in void inducing sub-micron particle properties such as inter-particle spacing and particle size in different orientations for the same material does not dominantly affect the fracture toughness.

Acknowledgements

The authors would like to thank Mr. Wolfgang Webersinke and Mr. Mario Houska for their contributions to the fracture mechanics testing of C(T) specimens, Ms. Gudrun Müller for her contributions to EBSD & SEM investigations and Ms. Michaela Rossner for metallographic preparations. Additional thanks to our colleagues at the workshop.

The use of the HZDR Ion Beam Center TEM facilities and the support by its staff is gratefully acknowledged. In particular, we gratefully acknowledge the funding of TEM Talos by the German Federal Ministry of Education and Research (BMBF), Grant No. 03SF0451 in the framework of HEMCP. This work contributes to the Joint Programme on Nuclear Materials (JPNM) of the European Energy Research Alliance (EERA).

References

[1] R.L. Klueh, P.J. Maziasz, I.S. Kim, L. Heatherly, D.T. Hoelzer, N. Hashimoto, E.A. Kenik, K. Miyahara, Tensile and creep properties of an oxide dispersion-strengthened ferritic steel, J. Nucl. Mater. 307–311, Part 1 (2002) 773–777. doi:10.1016/S0022-3115(02)01046-2.

[2] M.K. Miller, D.T. Hoelzer, E.A. Kenik, K.F. Russell, Stability of ferritic MA/ODS alloys at high temperatures, Intermetallics. 13 (2005) 387–392. doi:10.1016/j.intermet.2004.07.036.

[3] A. KIMURA, H.-S. CHO, N. TODA, R. KASADA, K. YUTANI, H. KISHIMOTO, N. IWATA, S. UKAI, M. FUJIWARA, High Burnup Fuel Cladding Materials R&D for Advanced Nuclear Systems, J. Nucl. Sci. Technol. 44 (2007) 323–328. doi:10.1080/18811248.2007.9711289.

[4] T.S. Byun, J.H. Kim, J.H. Yoon, D.T. Hoelzer, High temperature fracture characteristics of a nanostructured ferritic alloy (NFA), J. Nucl. Mater. 407 (2010) 78–82. doi:10.1016/j.jnucmat.2010.09.031.

[5] T.S. Byun, D.T. Hoelzer, J.H. Kim, S.A. Maloy, A comparative assessment of the fracture toughness behavior of ferritic-martensitic steels and nanostructured ferritic alloys, J. Nucl. Mater. 484 (2017) 157–167. doi:10.1016/j.jnucmat.2016.12.004.

[6] P. Dubuisson, Y. de Carlan, V. Garat, M. Blat, ODS Ferritic/martensitic alloys for Sodium Fast Reactor fuel pin cladding, J. Nucl. Mater. 428 (2012) 6–12. doi:10.1016/j.jnucmat.2011.10.037.

[7] R. Kasada, S.G. Lee, J. Isselin, J.H. Lee, T. Omura, A. Kimura, T. Okuda, M. Inoue, S. Ukai, S. Ohnuki, T. Fujisawa, F. Abe, Anisotropy in tensile and ductile–brittle transition behavior of ODS ferritic steels, J. Nucl. Mater. 417 (2011) 180–184. doi:10.1016/j.jnucmat.2010.12.069.

[8] M. Serrano, M. Hernández-Mayoral, A. García-Junceda, Microstructural anisotropy effect on the mechanical properties of a 14Cr ODS steel, J. Nucl. Mater. 428 (2012) 103–109. doi:10.1016/j.jnucmat.2011.08.016.

[9] A. García-Junceda, M. Hernández-Mayoral, M. Serrano, Influence of the microstructure on the tensile and impact properties of a 14Cr ODS steel bar, Mater. Sci. Eng. A. 556 (2012) 696–703. doi:10.1016/j.msea.2012.07.051.

[10] A.L. Rouffié, P. Wident, L. Ziolek, F. Delabrouille, B. Tanguy, J. Crépin, A. Pineau, V. Garat, B. Fournier, Influences of process parameters and microstructure on the fracture mechanisms of ODS steels, J. Nucl. Mater. 433 (2013) 108–115. doi:10.1016/j.jnucmat.2012.08.050.

[11] H. Hadraba, B. Fournier, L. Stratil, J. Malaplate, A.-L. Rouffié, P. Wident, L. Ziolek, J.-L. Béchade, Influence of microstructure on impact properties of 9–18%Cr ODS steels for fusion/fission applications, J. Nucl. Mater. 411 (2011) 112–118. doi:10.1016/j.jnucmat.2011.01.038.

[12] J. Hoffmann, M. Rieth, L. Commin, S. Antusch, Microstructural anisotropy of ferritic ODS alloys after different production routes, Fusion Eng. Des. 98-99 (2015) 1986–1990. doi:10.1016/j.fusengdes.2015.05.002.

[13] K. Arora, H. Viehrig, Evaluation of the ASTM and ISO J Initiation Procedures by Applying the Unloading Compliance Technique to Reactor Pressure Vessel Steels, Eval. ASTM ISO J Initiat. Proced. Appl. Unloading Compliance Tech. React. Press. Vessel Steels. (2011).

[14] ASTM Standard E1820-13, Standard test method for measurement of Fracture Toughness, (n.d.).

[15] Kim Wallin, Fracture Toughness of Engineering Materials - Estimation and application, EMAS Publishing, 2011.

[16] E. Aydogan, S. Pal, O. Anderoglu, S.A. Maloy, S.C. Vogel, G.R. Odette, J.J. Lewandowski, D.T. Hoelzer, I.E. Anderson, J.R. Rieken, Effect of tube processing methods on the texture and grain boundary characteristics of 14YWT nanostructured ferritic alloys, Mater. Sci. Eng. A. 661 (2016) 222–232. doi:10.1016/j.msea.2016.02.085.

[17] J. Chao, C. Capdevila, Anisotropy in Mechanical Properties and Fracture Behavior of an Oxide Dispersion Fe20Cr5Al Alloy, Metall. Mater. Trans. A. 45 (2014) 3767–3780. doi:10.1007/s11661-014-2329-7.

[18] A. Chauhan, D. Litvinov, Y. de Carlan, J. Aktaa, Study of the deformation and damage mechanisms of a 9Cr-ODS steel: Microstructure evolution and fracture characteristics, Mater. Sci. Eng. A. 658 (2016) 123–134. doi:10.1016/j.msea.2016.01.109.

[19] J.H. Kim, T.S. Byun, E. Shin, J.-B. Seol, S. Young, N.S. Reddy, Small angle neutron scattering analyses and high temperature mechanical properties of nano-structured oxide dispersion-strengthened steels produced via cryomilling, J. Alloys Compd. 651 (2015) 363–374. doi:10.1016/j.jallcom.2015.08.100.

[20] M. Praud, F. Mompiou, J. Malaplate, D. Caillard, J. Garnier, A. Steckmeyer, B. Fournier, Study of the deformation mechanisms in a Fe–14% Cr ODS alloy, J. Nucl. Mater. 428 (2012) 90–97. doi:10.1016/j.jnucmat.2011.10.046.

[21] M. Serrano, A. García-Junceda, R. Hernández, M.H. Mayoral, On anisotropy of ferritic ODS alloys, Mater. Sci. Technol. 30 (2014) 1664–1668. doi:10.1179/1743284714Y.0000000552.

[22] A. Das, H.W. Viehrig, F. Bergner, C. Heintze, E. Altstadt, J. Hoffmann, Effect of microstructural anisotropy on fracture toughness of hot rolled 13Cr ODS steel – The role of primary and secondary cracking, J. Nucl. Mater. 491 (2017) 83–93. doi:10.1016/j.jnucmat.2017.04.059.

[23] Pineau, Global and Local Approaches of Fracture -- Transferability of Laboratory Test Results to Components, Helmholtz-Zentrum Dresden-Rossendorf eV, 2011. https://inis.iaea.org/search/search.aspx?orig_q=RN:45041886 (accessed November 9, 2016).

[24] D.T. Hoelzer, K.A. Unocic, M.A. Sokolov, T.S. Byun, Influence of processing on the microstructure and mechanical properties of 14YWT, J. Nucl. Mater. 471 (2016) 251–265. doi:10.1016/j.jnucmat.2015.12.011.

[25] S. Pal, M.E. Alam, G.R. Odette, S.A. Maloy, D.T. Hoelzer, J.J. Lewandowski, Microstructure, Texture and Mechanical Properties of the 14YWT Nanostructured Ferritic Alloy NFA-1, in: I. Charit, Y.T. Zhu, S.A. Maloy, P.K. Liaw (Eds.), Mech. Creep Behav. Adv. Mater., Springer International Publishing, Cham, 2017: pp. 43–54. http://link.springer.com/10.1007/978-3-319-51097-2_4 (accessed September 5, 2017).

[26] M.E. Alam, S. Pal, K. Fields, S.A. Maloy, D.T. Hoelzer, G.R. Odette, Tensile deformation and fracture properties of a 14YWT nanostructured ferritic alloy, Mater. Sci. Eng. A. 675 (2016) 437–448. doi:10.1016/j.msea.2016.08.051.

[27] J. Han Kim, T. Sang Byun, D.T. Hoelzer, Stress relaxation behavior of nanocluster-strengthened ferritic alloy at high temperatures, J. Nucl. Mater. 425 (2012) 147–155. doi:10.1016/j.jnucmat.2011.06.040.

[28] J.H. Kim, T.S. Byun, D.T. Hoelzer, High temperature deformation mechanisms of nanostructured ferritic alloys in the context of internal variable theory of inelastic deformation, J. Nucl. Mater. 442 (2013) 458–462. doi:10.1016/j.jnucmat.2013.02.048.

[29] J.H. Kim, T.S. Byun, D.T. Hoelzer, C.H. Park, J.T. Yeom, J.K. Hong, Temperature dependence of strengthening mechanisms in the nanostructured ferritic alloy 14YWT: Part II—Mechanistic models and predictions, Mater. Sci. Eng. A. 559 (2013) 111–118. doi:10.1016/j.msea.2012.08.041.

[30] R.O. Ritchie, W.L. Server, R.A. Wullaert, Critical fracture stress and fracture strain models for the prediction of lower and upper shelf toughness in nuclear pressure vessel steels, Metall. Trans. A. 10 (1979) 1557–1570. doi:10.1007/BF02812022.

[31] R.O. Ritchie, A.W. Thompson, On macroscopic and microscopic analyses for crack initiation and crack growth toughness in ductile alloys, Metall. Trans. A. 16 (1985) 233–248.

[32] W.M. Garrison, N.R. Moody, Ductile fracture, J. Phys. Chem. Solids. 48 (1987) 1035–1074. doi:10.1016/0022-3697(87)90118-1.

[33] M.F. Ashby, Work hardening of dispersion-hardened crystals, Philos. Mag. 14 (1966) 1157–1178. doi:10.1080/14786436608224282.

[34] H.F. Fischmeister, E. Navara, K.E. Easterling, Effects of Alloying on Structural Stability and Cohesion between Phases in Oxide/Metal Composites, Met. Sci. J. 6 (1972) 211–215. doi:10.1179/030634572790445803.

[35] M.J. Alinger, G.R. Odette, G.E. Lucas, Tensile and fracture toughness properties of MA957: implications to the development of nanocomposited ferritic alloys, J. Nucl. Mater. 307–311, Part 1 (2002) 484–489. doi:10.1016/S0022-3115(02)01220-5.

[36] C.A. Williams, P. Unifantowicz, N. Baluc, G.D.W. Smith, E.A. Marquis, The formation and evolution of oxide particles in oxide-dispersion-strengthened ferritic steels during processing, Acta Mater. 61 (2013) 2219–2235. doi:10.1016/j.actamat.2012.12.042.

[37] J. Macías-Delgado, T. Leguey, V. de Castro, M.A. Auger, M.A. Monge, P. Spätig, N. Baluc, R. Pareja, Microstructure and tensile properties of ODS ferritic steels mechanically alloyed with Fe 2 Y, Nucl. Mater. Energy. 9 (2016) 372–377. doi:10.1016/j.nme.2016.09.019.

[38] L.J. Walpole, The elastic shear moduli of a cubic crystal, J. Phys. Appl. Phys. 19 (1986) 457.

[39] J. Turley, G. Sines, The anisotropy of Young's modulus, shear modulus and Poisson's ratio in cubic materials, J. Phys. Appl. Phys. 4 (1971) 264. doi:10.1088/0022-3727/4/2/312.

[40] J.M.J. Den Toonder, J.A.W. Van Dommelen, F.P.T. Baaijens, The relation between single crystal elasticity and the effective elastic behaviour of polycrystalline materials: theory, measurement and computation, Model. Simul. Mater. Sci. Eng. 7 (1999) 909.

[41] S.K. Yerra, C. Tekog˜lu, F. Scheyvaerts, L. Delannay, P. Van Houtte, T. Pardoen, Void growth and coalescence in single crystals, Int. J. Solids Struct. 47 (2010) 1016–1029. doi:10.1016/j.ijsolstr.2009.12.019.

[42] R. Chaouadi, G. Coen, E. Lucon, V. Massaut, Crack resistance behavior of ODS and standard 9%Cr-containing steels at high temperature, J. Nucl. Mater. 403 (2010) 15–18. doi:10.1016/j.jnucmat.2010.05.021.

[43] A. Pineau, A.A. Benzerga, T. Pardoen, Failure of metals I – Brittle and ductile fracture, Acta Mater. (2016). doi:10.1016/j.actamat.2015.12.034.

[44] A.S. Argon, J. Im, R. Safoglu, Cavity formation from inclusions in ductile fracture, Metall. Trans. A. 6 (1975) 825. doi:10.1007/BF02672306.

[45] G.R. Odette, Recent Progress in Developing and Qualifying Nanostructured Ferritic Alloys for Advanced Fission and Fusion Applications, JOM. 66 (2014) 2427–2441. doi:10.1007/s11837-014-1207-5.

[46] T.S. Byun, J.H. Yoon, S.H. Wee, D.T. Hoelzer, S.A. Maloy, Fracture behavior of 9Cr nanostructured ferritic alloy with improved fracture toughness, J. Nucl. Mater. 449 (2014) 39–48. doi:10.1016/j.jnucmat.2014.03.007.

[47] I. Hilger, F. Bergner, T. Weißgärber, Bimodal Grain Size Distribution of Nanostructured Ferritic ODS Fe–Cr Alloys, J. Am. Ceram. Soc. 98 (2015) 3576–3581. doi:10.1111/jace.13833.